Stony Brook University

The official electronic file of this thesis or dissertation is maintained by the University Libraries on behalf of The Graduate School at Stony Brook University.

Network Flow Modeling via Lattice-Boltzmann Based Channel Conductance. Prediction of Relative Permeability in Primary Drainage.

A DISSERTATION PRESENTED

BY

YELENA SHOLOKHOVA

TO

THE GRADUATE SCHOOL

IN PARTIAL FULFILLMENT OF THE REQUIREMENTS

FOR THE DEGREE OF

DOCTOR OF PHILOSOPHY

IN

APPLIED MATHEMATICS AND STATISTICS

STONY BROOK UNIVERSITY

August 2009

Stony Brook University

The Graduate School

<u>Yelena Sholokhova</u>

We, the dissertation committee for the above candidate for
the Doctor of Philosophy degree,
hereby recommend acceptance of this dissertation.

Professor Brent W. Lindquist, Advisor
Applied Mathematics and Statistics Department

Professor Yuefan Deng, Chairman of Defense
Applied Mathematics and Statistics Department

Assistant Professor Xiangmin Jiao
Applied Mathematics and Statistics Department

Associate Professor Troy Rasbury
Department of Geosciences

This dissertation is accepted by the Graduate School.

Lawrence Martin
Dean of the Graduate School

ii

Abstract of the Dissertation

Network Flow Modeling via Lattice-Boltzmann Based Channel Conductance. Prediction of Relative Permeability in Primary Drainage.

by

Yelena Sholokhova

Doctor of Philosophy

in

Applied Mathematics and Statistics

Stony Brook University

2009

We developed a set of models that allows accurate predictions of transport fluid flow properties of a suite of four samples of Fontainebleau sandstone ranging from 7.5% to 22% porosity, based on three-dimensional image analysis of its pore structure. We introduce three single-phase network flow models: one model is based upon Lattice-Boltzmann (LB) computations of each pore-to-pore connection; the second is based upon a power law fit to the relationship between computed conductance and throat shape factor; the third one uses conductances computed via standard pore body channel pore body series resistance (SR) with the conductance of each individual element (pore body, channel) based upon geometric shape factor measurements. The LB computations, based upon actual channel geometry derived from X-ray computed tomographic imagery, reveal that the variation in conductance for channels having similar shape factor is much larger than is adequately captured by the

geometric models. Bulk absolute permeabilities for Fontainebleau sandstone images are computed using the SR-based network model and the two LB-based models. Both LB-based network models produce bulk absolute permeability values that fit published data more accurately than the SR-based model. We then simulate the two-phase primary drainage flow properties on those network models incorporating actual geometry of throats for computing entry pressure arc meniscus radii and consequently throat entry pressures. We find that the description of throat geometries is particularly crucial in accurately predicting relative permeability curves that are in good agreement with experimental curves.

To all who pushed me and pulled me in my life.

Contents

List of Tables

List of Figures

Acknowledgements

Chapter 1

Introduction

Although the length-scale of an oil field is measured in kilometers, the ultimate success of an oil and gas recovery scheme is the net result of countless displacement events at a scale measured in microns [79]. Microscopic pore space structure of a porous medium controls the fluid transport of the reservoir rocks. Unfortunately there is no elegant mean-field theory, such as the multiple-continua model, to study the micro-structure of a porous material. As a consequence, the reliable microscopic rock models have to be evolved into an important tool for linking pore scale structure and bulk fluid properties at the scale of rock core samples by providing parametric relationships (such as capillary pressure - saturation or relative permeability - saturation) that are required in continuum-scale descriptions of multiphase flow. Such petrophysical parameters as relative permeability and capillary pressure are among the most important parameters used for reservoir management. They are used for reservoir characterization, reservoir engineering calculations, variables in numerical reservoir simulation models, determination of injectivities, productivities, water and oil coning behavior, and prediction of ultimate recoveries for various fluid injection schemes. Relative permeability investigations are also invaluable for predicting, identifying, and evaluating formation damage

that may result from a number of fluid or rock-fluid interactions [29]. Also for a successful hydrocarbon recovery or environmental remediation process the distribution of fluids in the pores must be fully understood and the appropriate mechanism for the fluid displacement constructed. All above mentioned applications require a wise development of the microscopic model which implements a level of abstraction of a medium, retaining only crucial features of the network, often in simplified form, while rejecting other parameters which play insignificant roles and can be neglected. Such parameter filtering is necessary since the models require storage and processing of huge amounts of data to characterize a tiny piece or rock [79]. For a example, Fontainebleau core samples analyzed in this study is of size $550 \times 550 \times 511$ voxel consist of around 155 million voxels. Considering that spatial resolution is $5.7 \mu m$/voxel these core samples are only 3.1mm on a side. Fontainebleau sandstone is rather a homogeneous type of rock having a constant grain size distribution over a wide range of porosities and therefore its Representative Element Volume (REV) in terms of porosity and permeability is small, approximately 1.3 mm cube side. For other rock types REV can be much larger and therefore would require more space and time to store and process them respectively.

Fig. 1 gives an insight into a microscopic world with comparison to the reservoir scale. In principle, any type of process that can be described at the pore scale can be incorporated in a network model to compute effective properties at a larger scale [8]. Such incorporation will be the major objective and core idea in this work:

1. Introducing two single phase pore network models based upon the LB conductance computations: one model is based upon LB computations for each pore-to-pore connection; the second is based upon a power law fit to the relationship between computed conductance and throat shape factor.
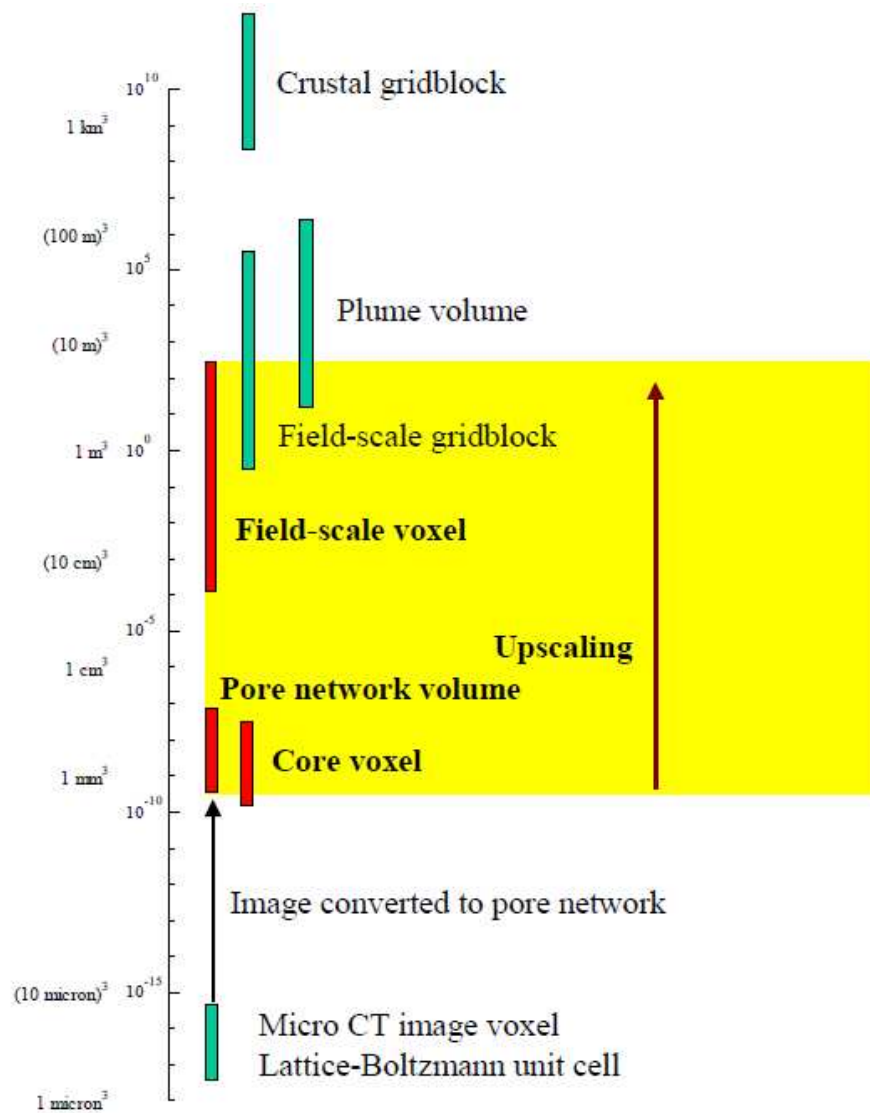
Figure 1: Characteristic volume scales in earth sciences. (Patzek, 2001)

2. Extending network models to two phase pore network models based on primary drainage throat geometry calculations [45].

3. Understanding Fontainebleau sandstone flow properties using single phase and two phase network models.

Network flow models [22, 23, 24, 9, 31, 32, 10, 14, 5, 36, 62, 17, 28, 7, 65, 66, 88, 37, 92, 49] and, more recently, Lattice Boltzmann models [76, 64, 20, 38] are the dominant numerical tools for simulating flow at the pore-scale level. Initially used for single phase computation, they are being utilized for increasingly complex flow simulations - multiphase, multicomponent, and reactive. In the progression to increasingly complex simulation, it is vital to continually assess the fundamentals of these numerical algorithms. In particular, network flow models capture a simplified description of a pore network, relying on computations based upon geometric assumptions to compute dynamic network parameters. A key advance in two-phase network flow modeling was enabled by the development of the ability to analytically compute entrance pressures for a tube of constant cross-sectional shape that is either triangular [62, 54] or regular polygonal [50]. Recently, this analytic ability has been extended to polygonal cross sections of arbitrary convex shape [45]. These advances have allowed modeling a degree of irregularity in channel cross sectional shape that was not available in earlier models which required circular or square cross sectional shape. Of particular benefit from this is the controlled modeling of film flow [62, 65]. There are various network flow models developed in the recent years. All of them share a common idea of simplifying the rigorous nature of pore structure and/or its hydrodynamic behavior so that these models retain its predictable properties at a specified degree of accuracy. Here we list all commonly used network flow models simplified at certain stages of its construction.

1.1 The Source of Pore Network

Usually network models represent the void space of a rock by a lattice of pores connected by throats. Until recently three different approaches were used to construct a network. In the first, the geometrical parameters of the lattice are tuned according to laboratory test data recorded from an experiment. In the second approach, rock formation processes (grain deposition, cementation and secondary geophysical and geochemical processes) are simulated to reproduce the 3D geometry of natural rock. In this approach, a grain size distribution obtained from thin section analysis is initially put into the reconstruction scheme, which then explicitly determines the random topology of a model by simulating dynamic geological processes. The second method is shown to produce very good prediction for relative permeability, unfortunately it is limited to sedimentary rocks. In our research group, we adopt a relatively new third approach for construction of three dimensional network flow model. It is undeniable that knowledge of rock geometry is limited by experimental tools. Prior to the development of high energy X-ray computed micro-tomography (CMT) in the late 1980's and its rapid improvement in the 1990's, experimental measurement of the distribution of any geometrical measure of pore space in rock was limited either to two dimensional thin sections, or to 3D views produced by thin sections stacks obtained laboriously through micro-polishing [47]. It is now possible to represent the complex geometry and topology of the pore space more accurately. Usage of X-ray computed tomography (XCT) to produce 3D image sets of rock samples, coupled with analysis software such as the 3DMA-Rock package [44], allows relatively rapid characterization of rock samples at the pore level, and the opportunity to incorporate greater geometric detail into network flow model descriptions. Geometrical analysis of XCMT images provides information on geometrical properties (and relationships between them) that are used as input to network flow models. This

geometric input is either in the form of the actual imaged network or in terms of geometrically equivalent (in a stochastic sense) networks.

1.2 Geometrical Characterization of the Pore Network

The extraction of the pore network in this study was performed using the software package 3DMA (see Stony Brook University Technical Report, SUNYSB-AMS-99-20 and the 3DMA-Rock home page at http://www.ams.sunysb.edu/~lindquis/3dma/3dma_rock/3dma_rock.html). The complete characterization of these algorithms is addressed in [45, 77, 89]. The main algorithmic procedures used to extract pore network information were:

1. Image segmentation by indicator kriging [61] to partition the image into void and grain phases (see Fig. 3). Other methods for segmenting gray-scale images are reviewed by Pal and Pal [63]. Methods reviewed include thresholding, iterative pixel classification based on relaxation, Markov random field or neural network based methods, edge detection, and a method based on fuzzy set theory [61]. More recently, several thresholding methods have been evaluated by Trier and Jain [86].

2. Construction of the medial axis [39] and extraction of its percolating backbone to provide a search path through the pore network. Medial axis is built using a skeletonization algorithm which is based on thinning method [39, 43]. Other skeletonization algorithms are based on analysis using maximal inscribed spheres [79] and on a catalog of shape primitives for 2D and 3D objects [35, 34].

3. Determination of throat locations (cross sections of locally minimum

area) in channels connecting pore bodies [46, 78, 71]; and identification of a pore body/throat network, where every pore body is cross-indexed with its connecting throats and adjoining pores [71].

1.3 Lattice-Boltzmann vs. Finite Difference Method

Recently, multiphase flow in porous media became a widespread topic in hydrologic research, motivated by contamination problems in soils. There are two types of multiphase network models which are conceptually different from each other: quasi-static displacement models and dynamic displacement models. We will study quasi-static models which go through a sequence of states: increasing/decreasing (drainage/imbibition) capillary pressures and the final, equilibrium positions of all interfaces in which dynamic aspects of pressure propagation are neglected. Dynamic models impose a specified inflow rate for one of the fluids and calculate the subsequent transient pressure response and associated interface positions [14].

From the point of view of computational tools for quantification of the relationship between micro-scale structure and fluid flow there are three types of tools: Lattice Boltzmann, network flow and smoothed-particle hydrodynamics (SPH) models which were initially developed for astrophysical and cosmological uses such as simulations of galaxy formation, star formation and stellar collisions but recently are being increasingly used to model fluid motion as well [59].

To bypass the problems associated with pore network extraction, fluid flow can be simulated directly on three dimensional segmented images of the rock space. One can either use a Lattice-Boltzmann method or finite difference

method. Lattice Boltzmann computation (e.g. [51, 64, 83, 90]) is exceptionally computationally demanding as it involves direct numerical simulation on a fully digitized representation of a porous medium [70]. The increment in the complexity between single-phase and two- or multi-phase flow is tremendous and formulation of no-slip or fixed-pressure boundary conditions may not be simple. However the Lattice-Boltzmann method is rather universal with respect to the range of phenomena suitable for numerical simulations. Another group of numerical simulations relies on a finite-difference approach [51, 52]. Making the assumption that the flow is steady and slow, one can eliminate the time derivative and the convective term in the flow equations. Both the finite-difference and the Lattice-Boltzmann methods lead to numerical solutions to the Stokes equations. Apparently there is no obvious winner between two approaches. Some finite-difference and Lattice-Boltzmann numerical schemes are very similar [27]. Despite all simplifying assumptions, pore network models remain a leading tool for understanding the physics of fluid flow and its relationship with pore morphology. Since the pioneering work of Fatt [22, 23, 24], who introduced the idea of network models, multiphase quasi-static models have been extensively studied by Celia [60, 14, 73], Øren [62], Blunt [87, 88, 7], Patzek [65, 79, 2, 66, 80] and others. Their models include only essential characteristics of a real rock core and in one way or another are reshaped for easier analysis purposes therefore do not necessarily reflect the pore space geometry of a particular rock. The major computational advantage of the pore network approach is the simplified treatment of the flow equations. The flow in the entire network is presented as a sum of flows in individual channels, called pore throats. In the pore bodies, which are the junctions of multiple throats, the mass balance equations yield an analog of the Kirchhoff's circuit law.

A third relatively new group of simulations of fluid transport is based

8

on smoothed-particle hydrodynamics. Particle methods such as smoothed-particle hydrodynamics are very robust and versatile for pore-scale flow and transport simulations, and it is relatively easy to add complex physical, chemical and biological processes into particle codes. For instance, a combination of standard SPH equations with pairwise fluid-fluid and fluid-solid particle-particle interactions allowed surface tension and three-phase contact dynamics to be realistically simulated [84]. The SPH method is used not only in multiphase flow modeling but also in reactive transport modeling as a part of a multi-scale numerical and experimental study of mixing-induced reactions and mineral precipitation. However, the computational efficiency of particle methods is low relative to continuum methods. Two-dimensional models are still predominant in SPH methods. Multi-scale particle methods and hybrid (particle-particle and particle-continuum) methods may be needed to improve computational efficiency and make effective use of emerging computational capabilities.

1.4   Single-Phase Pore Network Conductance

Pore throats play a role of a dam which regulates a fluid flow and is of utmost importance in pore structure responsible for such hydrologic properties of rock as conductance/permeability. It is important to note that our characterization is a pore body/throat network and not a pore body/channel network. Each throat is constructed as a surface of contact between two pore bodies. These surfaces are triangulated, not necessarily planar, polygons. The surfaces occupy no volume; all the volume of the pore network is in the pore bodies. A fundamental quantity required for any network flow model is the conductance governing the flow between any two connected pore neighbors in the

network. For rectangular and elliptical cross-sections, the effective conductance governing incompressible, low-Reynolds number, Navier-Stokes, single phase flow can be computed analytically [65]. For a regular polygon or irregular triangle cross section shape, numerical computations are required [62] to compute conductances. These computations show that a monotonic relation exists between the dimensionless conductance and a dimensionless shape factor [54] that characterizes each of these shapes. This monotonic relation can be pre-computed and, in the case of numerically computed relations, fit to an accurate analytic form which is then used in the network flow model. These shape factor-conductance relationships perfectly capture the spirit of network flow models - namely to extract critical, relatively simple, experimentally accessible measures of the pore network geometry that can be used to develop accurate network flow models.

Oren [62] and Patzek [65] have described network flow models based upon these shape factor-conductance relationships. These models are standard, in that pore to pore conductance is computed via a pore body-channel-pore body series resistance (SR), with the conductance of each individual element (pore body, channel) based upon measurements of shape factor. The cross sectional shapes of the network elements (pore bodies, channels) are determined by fitting to shape factor data taken from simulated or real media. While triangular shapes have been a desired feature of these models, due to limitations on the range of shape factors available for triangles, cross sections in these models are augmented with rectangular and elliptical cross sections to model the broader range of shape factors observed in real porous media. In §3, in the context of single phase flow, we review these shape factor-conductance relationships and the network flow models based upon these relationships.

The conductance estimates based upon shape factor work surprisingly well in spite of the introduction of potential "peculiarities" in the geometry of the

10

pores. In the triangular cross-section models, the conductance computation for each pore-channel-pore connection assumes constant cross sections of triangular shape separately for each of the two types of elements (pore, channel) forming the connection. Thus pores and channels are effectively modeled as triangular prisms. While this is conceptually acceptable for channels, it is difficult to reconcile the geometry of a pore which has the same triangular prism shape in *every* direction to which it connects to a neighboring pore.

For modeling flow through real media, use of X-ray computed tomography (XCT) to produce 3D image sets of rock samples, coupled with analysis software such as the 3DMA-Rock package [44], allows relatively rapid characterization of rock samples at the pore level, and the opportunity to incorporate greater geometric detail into network flow model descriptions. In §2, we summarize the XCT analysis of four Fontainebleau data sets, ranging from 7.5% to 22% porosity, used in this study.

Of particular interest to us is the detailed geometry of the connection between any two neighboring pores and the effect of approximating this geometry when computing effective pore-to-pore conductance. We compare three methods of computing pore-to-pore conductance. The first (§3.1) is a series resistance model utilizing conductances estimated from shape factors (G) and triangular/rectangular/elliptical geometries. We refer to this method as SRG. In the second method (§3.3), we utilize a Lattice-Boltzmann (LB) model to compute an accurate approximation to Navier-Stokes flow through each isolated pore-to-pore connection in the Fontainebleau data sets and determine a connection-specific conductance. We refer to this method as LBC. This method, which involves running an LB computation separately on each channel is CPU intensive. We therefore consider a third method where pore-to-pore conductances are computed using an analytic expression obtained from the fit between LBC computed conductances and throat shape factors, G. We refer

11

to this third method of computing pore-to-pore conductances as LBG.

In §3.4 we compare the results for computing the effective (i.e. bulk) absolute permeability for the four sandstone networks using network flow models based upon the three methods for estimating pore-to-pore conductance. The first network flow model (NF-SRG), which closely follows the work of Oren [62] and Patzek [65], utilizes the SRG method for estimating pore-to-pore conductance. We also investigate the sensitivity of the NF-SRG model to the weighting of the elements in the series resistance of each pore-to-pore connection. The second model (NF-LBC) directly uses the LBC computed conductances. This model eliminates the need for both series resistance and cross-sectional geometry approximation in the computation of the pore-to-pore conductances. The third model (NF-LBG) uses the LBG method for computing pore-to-pore conductance. Use of NF-LBG eliminates the need for series resistance approximation. All models are validated against published measurements [12].

1.5   Multiphase Fluid Flow

The study of multiphase flow in porous media is of major interest in oil recovery and contaminant remediation in aquifers [70]. Relative permeability and capillary pressure are mesoscopic transport properties that describe the simultaneous flow of immiscible (incapable of being mixed) fluids in porous media [13]. The relative hydrodynamic conductance of each fluid at a given saturation is the relative permeability, while the pressure difference between the phases is the capillary pressure. These two functions determine the macroscopic fluid flow behavior in reservoirs [13]. To predict the behavior of these two functions we need to take into account the following factors: pore space geometry, viscous forces, surface tension and contact angle. Note that the displacement of two fluids is particularly dependent on the pore space geometry

12

which emphasizes the need of pore space characterization. In §4 we overview basic concepts of immiscible fluid displacement and introduce two types of models: MS-P and VRONI. Initially a sample is fully saturated with a wetting fluid. Non-wetting fluid is allowed to access a network through one side (INLET) either in x-, y- or z- direction and exit an opposite side (OUTLET) while other four sides are sealed. All pores on the INLET boundary of the pack are filled with non-wetting fluid at the beginning of a drainage and the rest of pores and throats are filled one at a time during the process. A throat is considered available if it does not contain injected fluid but is connected to a pore body that does. At each stage the available throat with the smallest entry capillary pressure P_{entry} is filled together with all empty (filled with wetting fluid) pores connected to it. MS-P and VRONI models use different throat entry pressures. In the MS-P model threshold or entry capillary pressures are calculated with the Mayer and Stowe [55] and Princen [67, 68, 69] method. The VRONI model utilizes computed entry radii r_e for throats which are represented by simple connected polygonal shapes obtained by the 3DMA-rock software package and analyzed via the computational geometry theory of medial axis [45].

Validation of the predictive capability of network flow models requires comparison with experimental measurements on fluid flow patterns at micro- and macro-scales [70]. To test and validate our network model for the case of two-phase simulations of water wet conditions, we considered four samples with different petrophysical properties to perform pore-level calculations. We used experimental gas/oil drainage relative permeability curves for a sandstone reservoir for comparison with numerical calculations. Experimental samples were from fairly clean (low clay) homogeneous well-sorted sandstone plugs from a shallow marine depositional environment obtained by Sorbie *et al.* [56] and

13

are similar to Fontainebleau sandstone characteristics. The calculated permeability and capillary pressure is in good agreement with the corresponding laboratory measurements. Our simulations show that in two-phase pore-scale models the accurate calculations of throat entry radii and throat wetting areas are responsible for pore network predictive capabilities.

1.6 Contribution

Most models of the pore space of a porous solid are based on some form of bundles of capillary tubes with constant cross-sections [14]. While use of tubes allows simple analytical formulas to be derived for single-phase and multi-phase fluid flow properties such as hydraulic conductance, relative permeability, such models miss a fundamentally important geometrical characteristic of porous solids, namely pore-to-pore complexity of a channel shape that is responsible for an accurate prediction of the channel conductance in computing bulk absolute permeability or threshold pore entry pressure in primary drainage. Therefore we concentrated on the description of a pore-to-pore connection in our pore network models and introduce three pore network models that better reflect rigorous pore space microstructure. We tested their predictive abilities by comparing each model against published data. The single-phase pore network models we developed are:

1. NF-SRG model utilizing conductances estimated from shape factors (G);

2. NF-LBC model utilizing computation of conductances by simulating an accurate Navier-Stokes flow through each isolated pore-to-pore connection;

3. NF-LBG model where pore-to-pore conductances are computed using an analytic expression obtained from the fit between LBC and G;

We then developed a primary drainage pore network model in which threshold pore entry pressures are computed using actual throat geometries. While pore-scale network models are more involved and detailed than other possible approaches [14], we believe that our models offer significant understanding of fundamental fluid behavior in porous media and, more important, they offer possibilities for improvements in predictive capabilities for difficult multi-phase flow problems currently facing us.

Chapter 2

Fontainebleau sandstone data

Fontainebleau sandstone has advantages and disadvantages as a study rock. From one point of view, it is used as the ideal experimental system to test and validate pore-level numerical studies. Its composition is 100% quartz which is well sorted and the grain size is around 250 μm. The variation of porosity is enormous and goes from 2% to 30% without noticeable grain size modification. Such rather unusual sandstone properties allow us to study the effects of porosity and micro-structure independently of every other parameter [12]. From the negative point of view, Fontainebleau sandstone is a highly homogeneous sandstone which does not contain clay and only displays intergranular porosity [3]. In addition, since it is completely water wet it is impossible to investigate the effect of porosity on distribution of irreducible wetting-phase saturation [33] and conduct contact angle analysis. In the section §2.1 we overview typical properties of Fontainebleau microstructure and in §2.2, §2.3, §2.4, §2.5 we investigate the morphology of four samples used in the study.

2.1 General properties of Fontainebleau sandstone

The transport properties of rock depend critically on the geometry of pore space and therefore it is required to have full analysis of pore structure for quantitative understanding of permeability and its relationship to pore morphology. Fontainebleau sandstone is essentially formed of quartz grains that have undergone long-term erosion and good grain size sorting before being deposited, during the Stampian, in dunes bordering the shore (Oligocene, Paris Basin). Following a geological evolution, still not fully understood, these sands underwent cementation (more or less intensive) by silica, which crystallized around the grains in the form of quartz in crystalline continuity with them. Fontainebleau sandstone thus displays exceptional chemical (fully water-wet) and crystallographic simplicity [11]. Because of simplicity of grain phase the associated intergranular space is also simple (Fig. 2, 3). For comparison, Fig. 4 by Bourbie *et al.* displays other rock materials, in which that pore space can be very complex. In addition to this intrinsic complexity of commonly found pore spaces is the problem of the three-dimensionality of pore spaces as opposed to the two-dimensionality of means of observation and analysis [11].

2.2 Quantitative Analysis of Pore Space Geometry

Here we present quantitative micro-structural characterization of the pore geometry for four samples. The network models constructed in this study are based upon an analysis of Fontainebleau sandstone samples with porosities of 7.5, 13, 18 and 22%. The XCT images, digitized at 5.7 μm voxel size, were
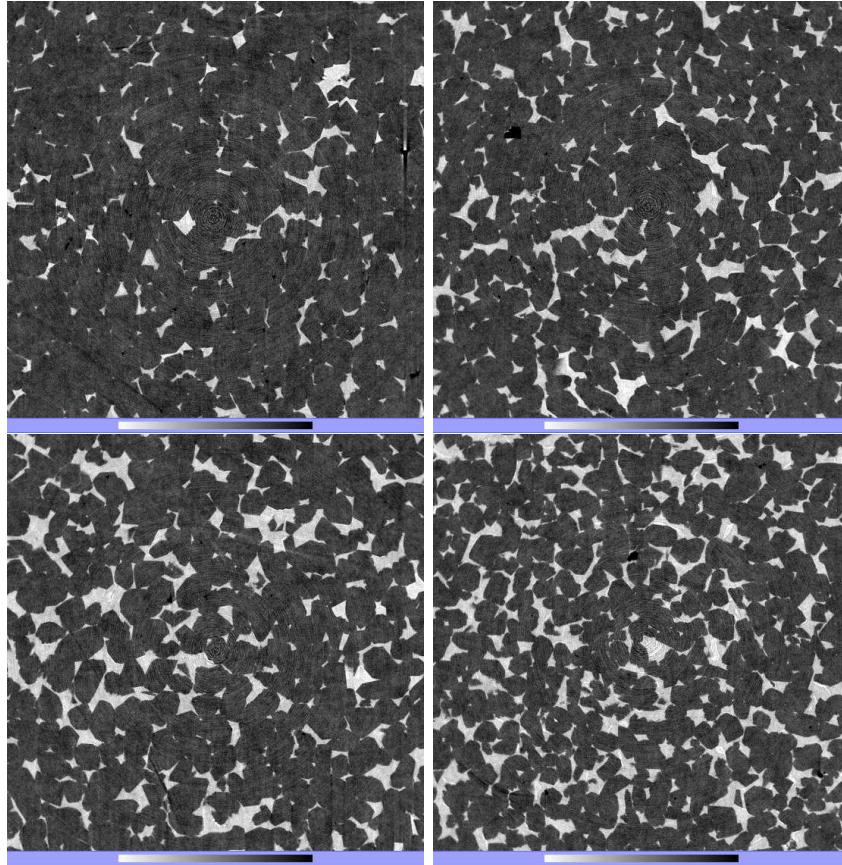
Figure 2: Single slices from the XCT image of the 7.5%, 13%, 18% and 22% Fontainebleau sandstone sample analyzed by 3DMA-Rock.
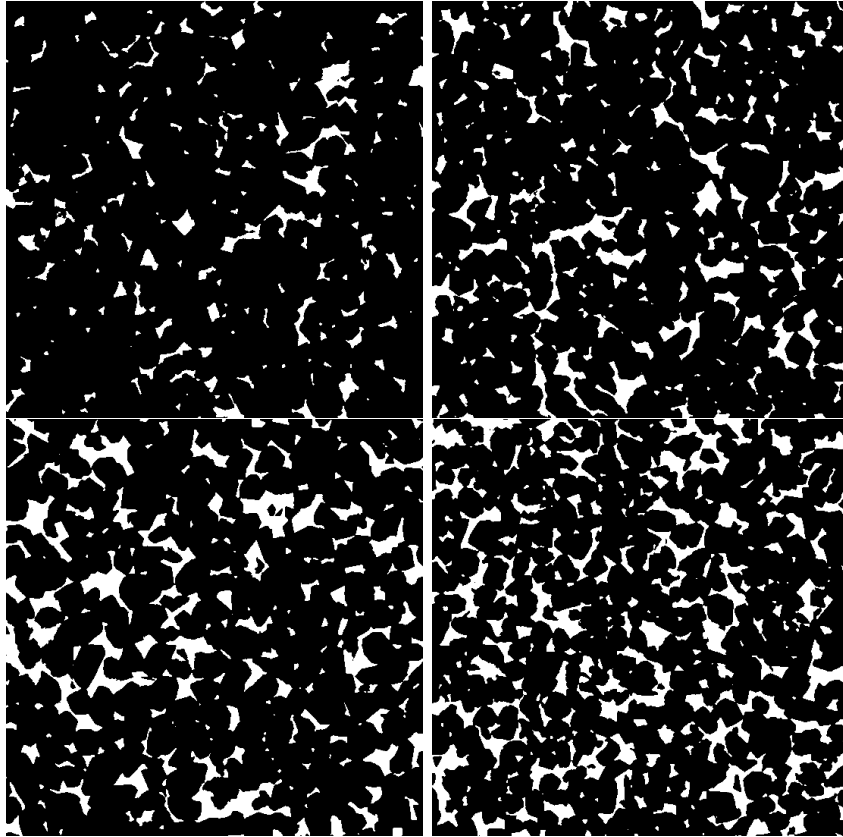
Figure 3: The same slices after segmentation of the image via the indicator kriging algorithm in 3DMA-Rock.

500 μm

500 μm
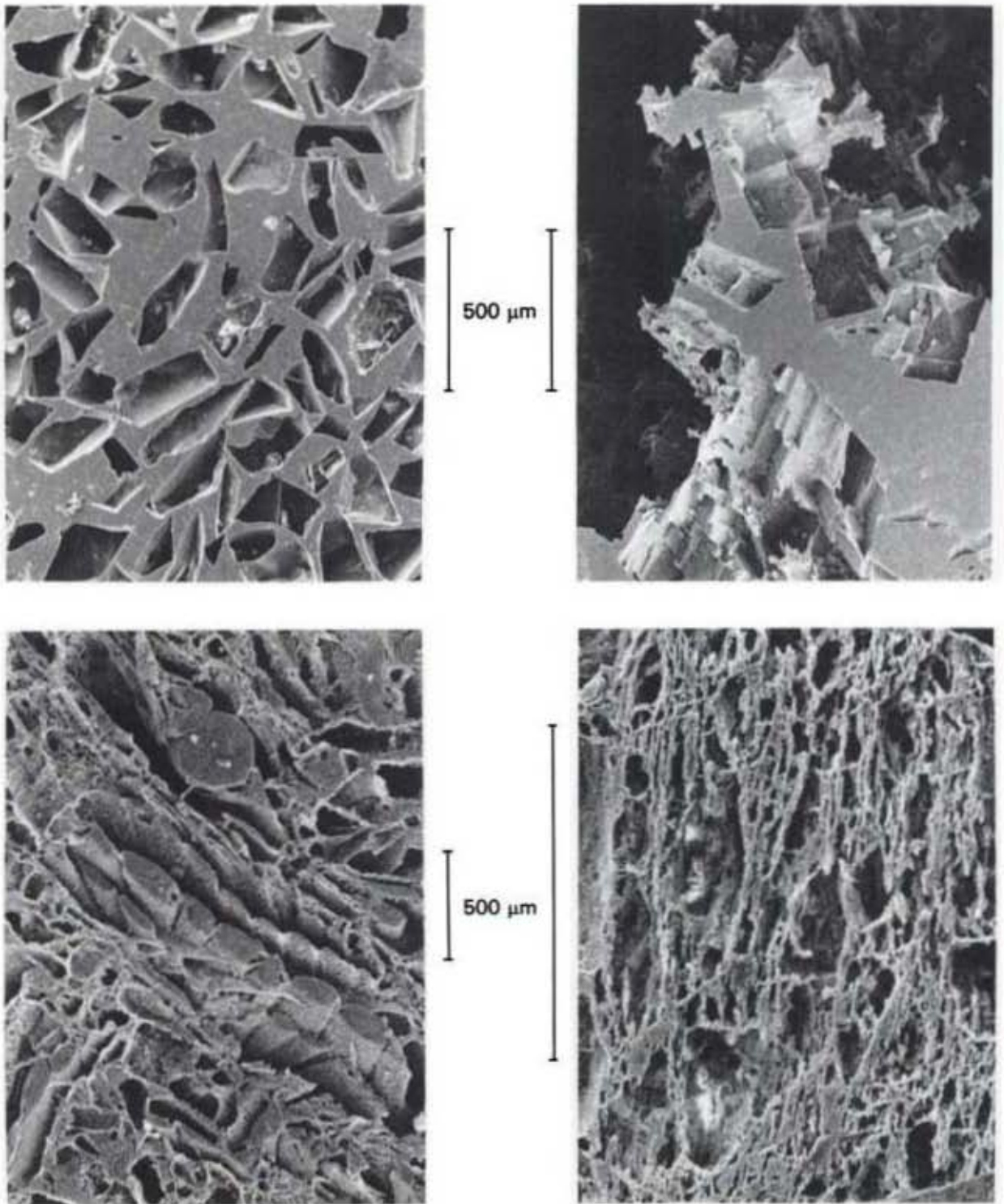
Figure 4: Ground Pyrex (left, top), Vuggy dolomite (right, top), Nummulite
Limestone (left, bottom), Altered Feldspath (right, bottom). (Bourbie *et al.,*
1987)

taken of cores 5 mm in diameter at the X2B beam line at the National Synchrotron Light Source at Brookhaven National Laboratory. From each image, a $550 \times 550 \times 511$ voxel (28.63 mm^3) rectangular subvolume was analyzed by 3DMA-rock software. The main algorithmic procedures are described in §1.2. The full analysis can be found in [43, 75, 3, 81, 82, 46, 47, 42].

2.3 Coordination Number and Channel Length

Coordination number is one of essential parameters of pore space since the connectedness of pore throats control the flow properties. Coordination number is attributed to a pore and tells how many pores are connected to it. The 4 distributions determined from each core sample where then averaged, and are presented in Fig. 5 on the left. The range $3 \leq C \leq 9$ consistently displays an exponential distribution, $10^{-C/\lambda_C}$, both for the individual subcores, and for the 4-subcore averages [47]. It is important to note that since the distributions are exponential, the characteristic coordination number λ_C is the actual descriptor of the distribution and not the average coordination number C. The average lies between 3 and 4, rising approximately 11% over the porosity range examined and therefore this fact can lead to a wrong conclusion that samples connectivity remains the same over porosity range. From Fig. 8 we see a linear increase of the form $\lambda_C(\phi) \sim 0.073(6)\phi$ in the value of the characteristic coordination number λ_C with porosity ϕ over the range. However there is the observed trend for the coordination number to decrease with decreasing porosity and increasing cementation, the void space in Fontainebleau sandstone remains a continuous network to very low porosity. Why this happens can be explained from the thorough further investigation. The topology of rock is not seen from two-dimensional slices depicted in Figs. 2, 3 and proves that

only three-dimensional analysis can shed light on true pore micro-structure. Even though a two-dimensional image can mislead someone it still carries a lot of information. Analyzing a large porosity sample (Fig. 2, 3) one can see that grains are weakly cemented having small contact areas while a low porosity sample is tightly composed having longer pore/throat channels but not necessarily narrower.

As noted before from examing segmented images (Figs. 2, 3) that low porosity samples have longer pore/throat channels. This fact can be quantified by constructing the pore channel length distribution and observing the strong exponential decay character of the distribution as the porosity increases. The increase of pore channel length with decreasing porosity is an indication of the previously denoted fact of existence of conductivity at low porosity, longer channel lengths between fewer pores have to be maintained [43]. The results of the fits for the 4-subcore averaged distributions are summarized in Fig. 5 [47].

2.4   Pore and Throat Size Distributions

Both pore and throat measurements contribute to the understanding of fluid flow properties: large pores account for most of rock porosity and it is well known that porosity is directly related to the rock permeability while throats/pore channels control the fluid displacement.

The measured distribution of throat areas is exponentially distributed $10^{-\frac{A}{\lambda_A}}$, where λ_A is the characteristic throat area and A is the throat cross sectional area (Fig. 6). There is indication of an increase in the characteristic area λ_A with porosity. The distribution of nodal pore volumes appears to be log-normal (Fig. 7). The values of ln(V) slightly decrease with porosity. In summary, the relatively minor changes in the characteristic throat area and

22
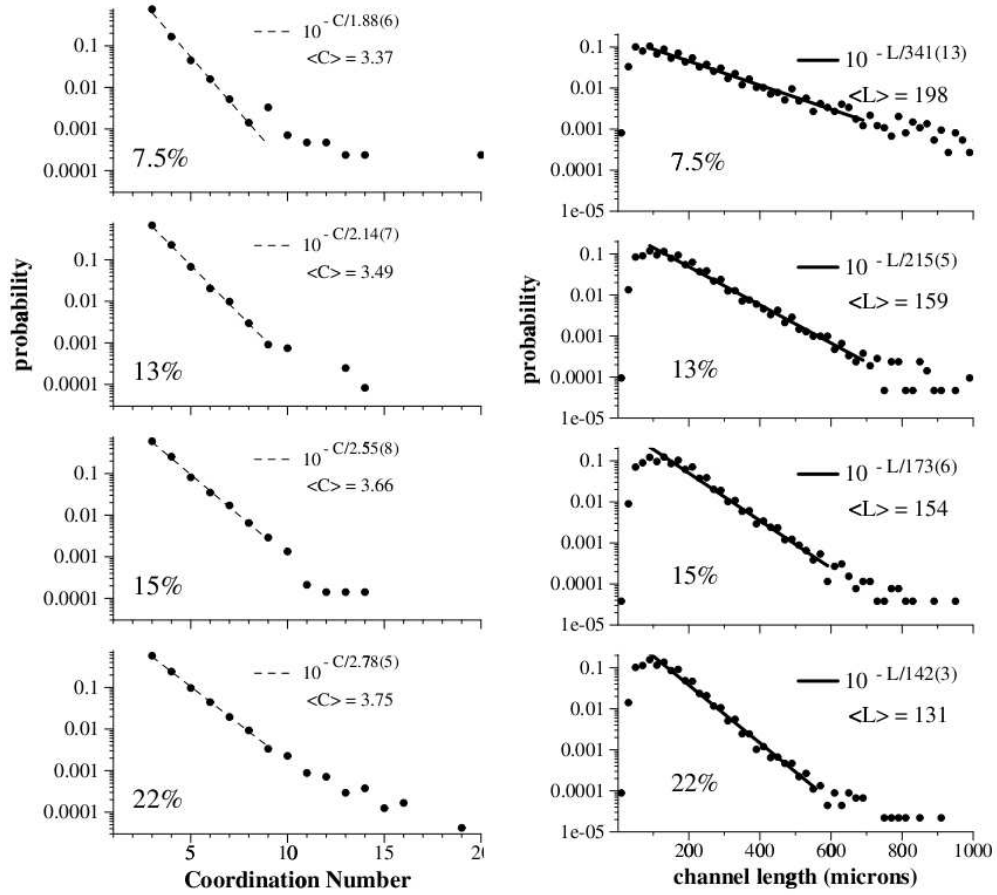
Figure 5: Measured distributions of coordination number (left) and pore channel lengths (right) for cores taken from Fontainebleau sandstone of 7.5%, 13%, 18% and 22% bulk porosity. (Lindquist *et al., 1999*)
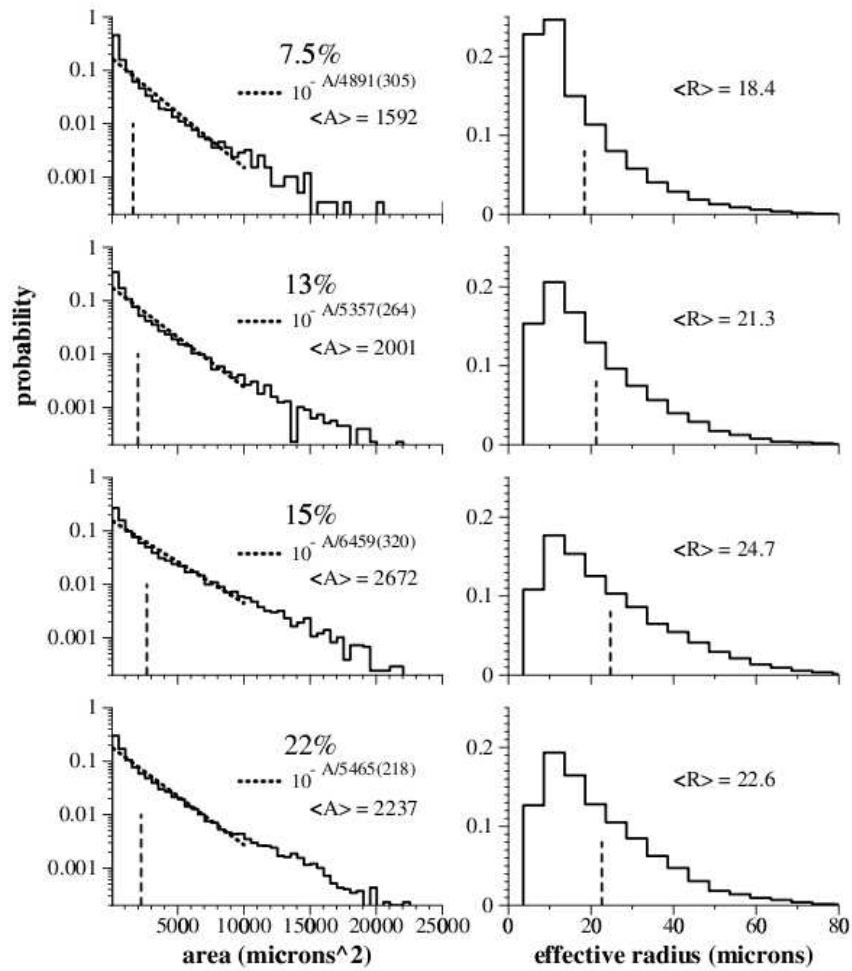
Figure 6: Measured distributions of throat cross sectional areas (left) and effective throat radius (right) (assuming circular areas) for cores taken from Fontainebleau sandstone of 7.5%, 13%, 18% and 22% bulk porosity. (Lindquist *et al., 1999*)

24
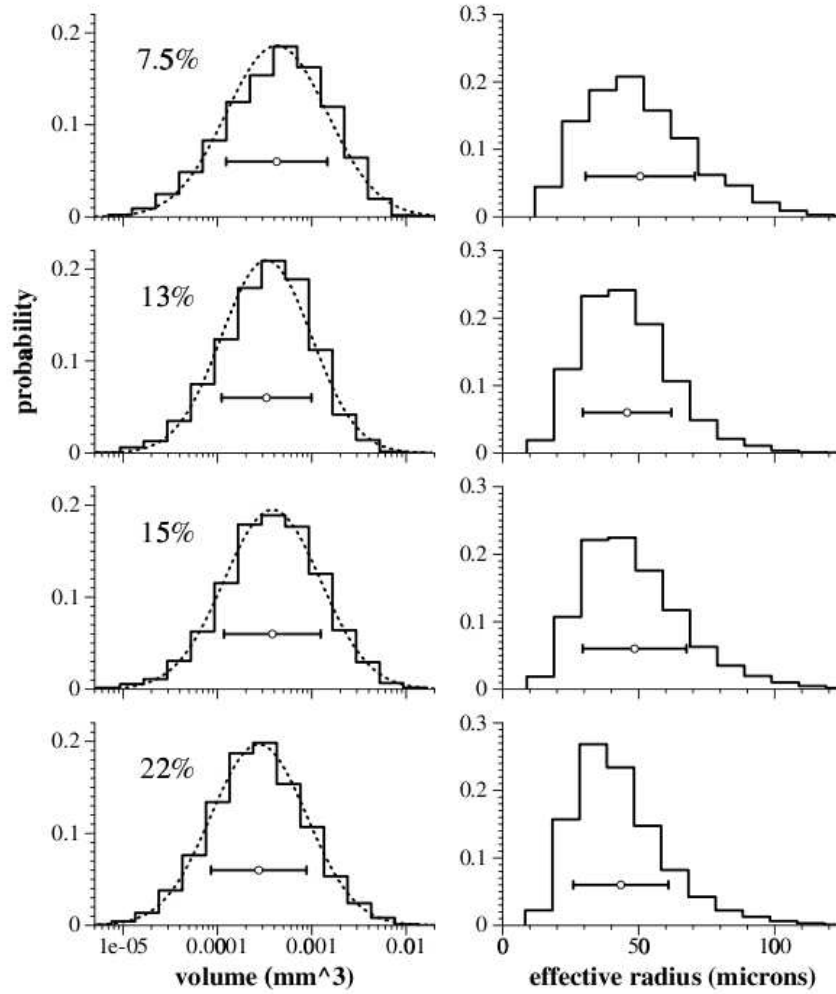
Figure 7: Measured distributions of nodal pore volumes (left) and effective pore radius (assuming circular areas) (right) for cores taken from Fontainebleau sandstone of 7.5%, 13%, 18% and 22% bulk porosity. (Lindquist *et al., 1999*)

average logarithm of nodal pore volume reveal a universality of expansion of channels and nodal pores over dimensional ranges [47]. Figure 8 displays dependence of characteristic distribution parameters on measured porosity, over the range 7.5%, 13%, 18% and 22% for Fontainebleau sandstone. Note that measurements for 15% porosity sandstone block are a bit off the trends. This may be related to the fact that it comes from a slightly anomalous section of the core of 18% porosity.

2.5   Tortuosity

The hydraulic tortuosity factor Υ is introduced in most of permeability models (example: Carman-Kozeny or Mean Hydraulic Diameter Model). The tortuosity of a porous medium is a fundamental property of the streamlines, or flux, in the conducting capillaries [21] and describes a network complexity in porous media. It is defined as $\Upsilon = L_e/L$ where L is a sample length in the direction of macroscopic flow and L_e is an average effective path length and $L_e > L$. It is observed in Figs. 9, 10 that the tortuosity in the low porosity sample is abnormally high and variation is large compared to the rest of the samples which means that the fluid has to follow more complicated paths to get through the porous medium.

Tortuosity depends on various rock parameters: the shape, size, and type of the grains, pores, and pore channels; mode of packing of the grains; grain size distribution; the orientation; and nonuniformity of the grains [74]. We see a positive correlation between the channel length and tortuosity: there is a characteristic channel length decay with tortuosity decrease over the range of porosities. We also observe that variation in tortuosity values over the range of porosities is correlated with the variation of effective radii of pores: wider distribution of pore effective radii replicates with wider distribution of
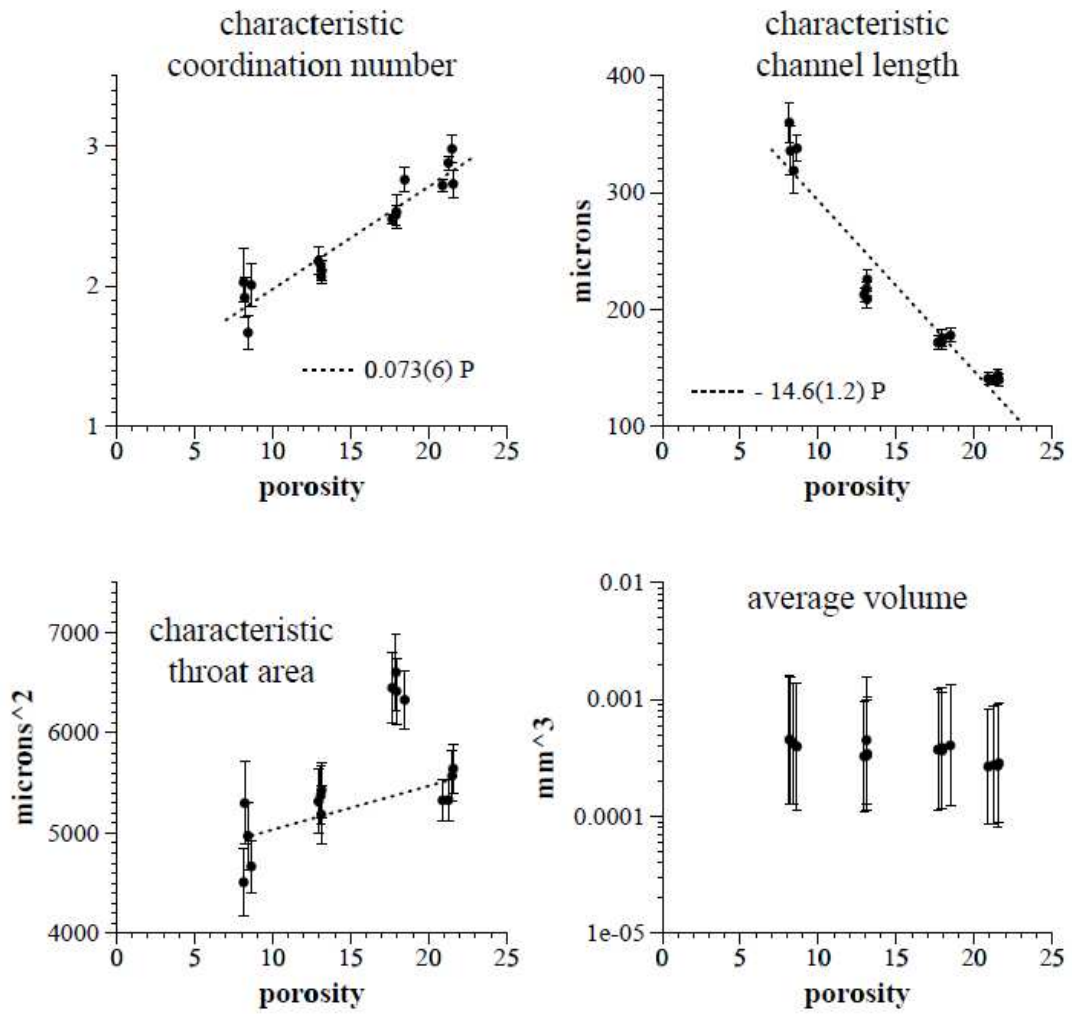
Figure 8: Dependence of characteristic distribution parameters on measured porosity for cores taken from Fontainebleau sandstone of 7.5%, 13%, 18% and 22% bulk porosity. (Lindquist *et al., 1999*)

Fontainebleau 7.5%, x-dir

• density   —— cumulative

face 3 --> 4 (av 2.26907)

shortest paths (av 2.35262)

Fontainebleau 13%, x-dir

• density   —— cumulative

face 3 --> 4 (av 1.7302)

shortest paths (av 1.68507)

tortuosity

Fontainebleau 15%, x-dir

• density   —— cumulative

28

face 3 --> 4 (av 1.65394)
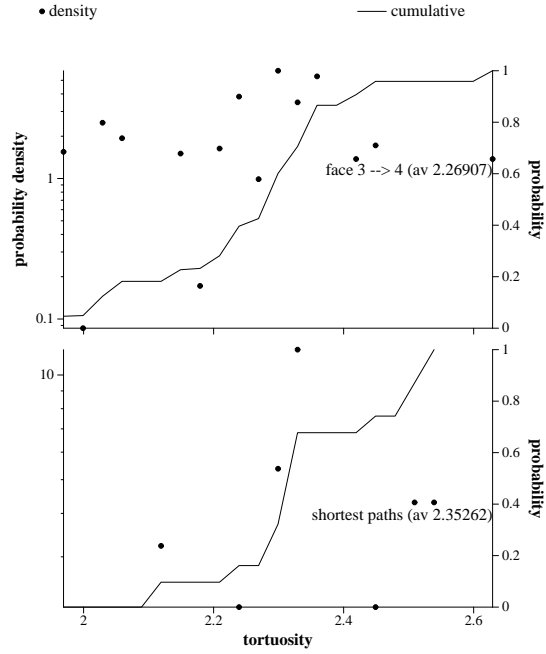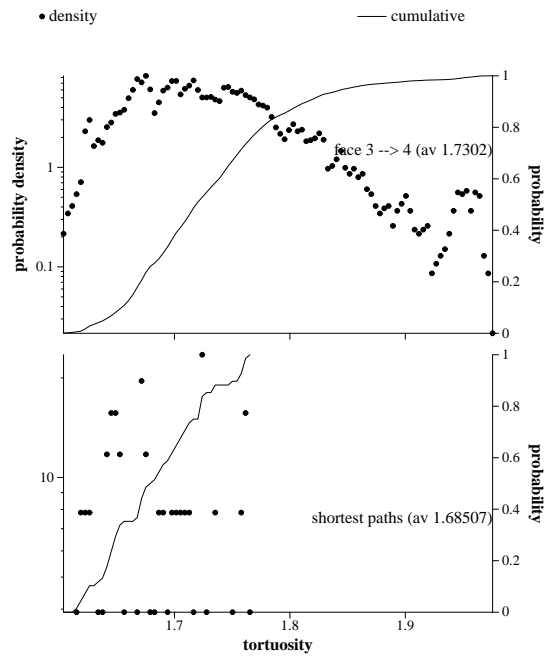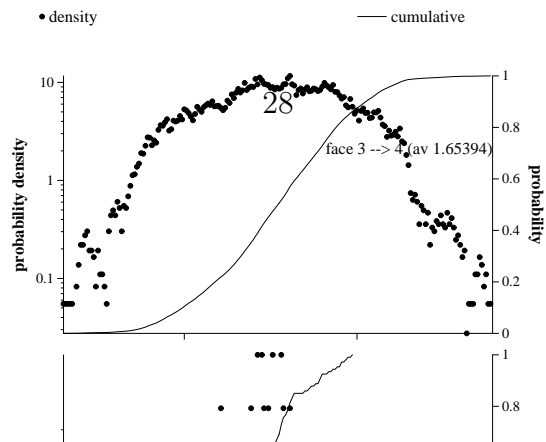
tortuosity values (Figs. 7, 9).
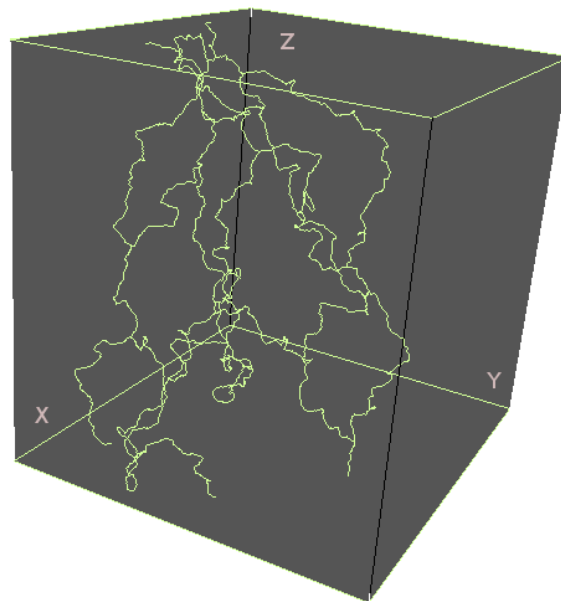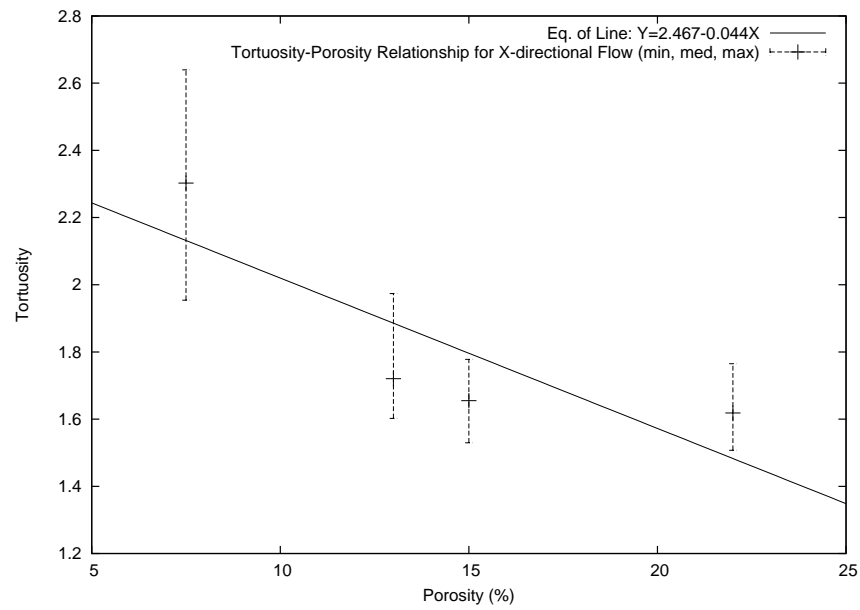
Figure 10: Tortuosity versus porosity relationship for cores taken from Fontainebleau sandstone of 7.5%, 13%, 18% and 22% bulk porosity (top). Geomview plot of the shortest medial axis paths for 7.5% porosity sample (bottom).

Chapter 3

Single-phase pore networks

It is now possible to represent the complex geometry and topology of the pore space more accurately. Knowledge of rock geometry is limited by experimental tools. Now by the means of CMT, together with image analysis packages such as 3DMA-Rock, CMT images can be analyzed and accurate description of geometry and topology can be recovered to make accurate 3D predictions. Although the 3DMA-Rock software enables construction of an accurate 3D pore network, simplification of pore geometry takes place when we build a topologically equivalent network model, since use of simplifying geometrical features allows analytical formulas to be applied for macroscopic properties. So, the first challenge of pore scale modeling is to determine the details in the description of pore space necessary to make accurate predictions. The second challenge is to find an idealized representation which will keep all essential features and be easy enough for analytical analysis. Mason and Morrow [54] introduced a new characteristic of a pore, named a shape factor and related it to the triangular shape which would represent the pore shape, replicating the significant features of it. Angular corners retain wetting fluid and allow two or more fluids to flow simultaneously through the same pore [62] at a given time. Smooth pores have high shape factors and will be represented

with circular cross sections, whereas more irregular pore shapes will be represented by triangular cross sections [7]. The assumption is that the triangular shape reproduces correctly the roughness of pore, and correctly balances the amount of wetting fluid and non-wetting one. Thus the triangularity of pores is essentially important for building reliable multi-phase models investigated in Chapter §4. Here we describe and compare various single-phase models based not only on idealized shapes of channels, SRG, (§3.1) but also on actual geometries, LBC, (§3.3) provided by 3DMA-rock software. We utilize a second model by introducing a third model, LBG, based on analytic expression obtained from fit and described in details in §3.3. We then analyze its predictive properties by comparing the results of all three models with experimental curve of Bourbie *et al.*.

3.1   Hydraulic conductance based upon series resistance: the NF-SRG models

The volumetric flow rate of an incompressible fluid flowing with constant viscosity in a duct is described through the solution to the elliptic Poisson equation

$$\nabla^2 \overrightarrow{\nu} = \frac{1}{\mu}(\nabla p - \rho \overrightarrow{f})$$

(1)

with boundary condition $\nu(x_1, x_2) = 0$ on Γ_s, the duct wall, where $\overrightarrow{\nu}$ is the fluid velocity, $\overrightarrow{f}$ is the body force per unit mass (i.e. the gravity), μ is the fluid viscosity, and ρ is its density. Choosing the x_3-axis as parallel to the axis of the duct, pressure gradient ∇p generates a flow in the x_3 direction, and the gravity can be neglected. The solution to Poisson equation, the velocity distribution function, relates the volumetric flow rate to the gradient pressure.

$$Q = \langle \nu \rangle A = -g(\nabla p)$$

(2)

Darcy's law is another view on Poisson equation. The single phase flow rate between neighboring pore bodies i and j in a network flow model is described by Darcy's law,

$$Q_{ij} = \frac{g_{ij}}{l_{ij}}(p_i - p_j),\qquad(3)$$

where Q_{ij} is the volumetric flow rate [L^3/T], g_{ij} is the effective fluid conductance [L^{5}T/M], l_{ij} is the distance between the pore centers, and p_i is the pressure (at the CoM) of pore i. A standard computation for the effective fluid conductance, g_{ij}, is the harmonic mean of the conductances of the connecting channel and the two pore bodies

$$\frac{l_{ij}}{g_{ij}} = \frac{l_c}{g_c} + \frac{1}{2}\left[\frac{l_i}{g_i} + \frac{l_j}{g_j}\right],\qquad(4)$$

where the subscript c stands for channel. The lengths l_α, $\alpha = i, j, c$, associated with pore bodies, i and j, and the connecting channel, c, satisfy

$$l_{ij} = l_c + \frac{1}{2}(l_i + l_j).\qquad(5)$$

The lengths l_α, $\alpha = i, j, c$ and the corresponding conductances g_α must be modeled.

When information on the network is extracted from real rock (e.g. by analysis of XCT images), network models implementing the SR formulation employ different strategies for determining the effective length l_c, i.e. for determining "where a pore ends and the connecting throat channel begins". From this perspective, the choice of l_c is thus an adjustable parameter in (5). The two other lengths l_i and l_j adjust accordingly to compensate for total pore-to-pore length restriction. We believe that the sensitivity of network flow models to the strategy for determining the pore/channel element weighting in the SR formulation has not been fully addressed in the literature. As one aspect of this work, we study the sensitivity of SR formulations to such strategies by employing the following single parameter formulation.

We begin by noting that the pore/throat description of pore space adopted by 3DMA-Rock is unambiguous in the sense that the definition of a throat, as the cross section of minimum area connecting two neighboring pores, is well defined (as opposed to any definition of the location where the pore space transitions from pore body to connecting channel). We therefore adopt the following approach to computing effective channel conductances in the implementation of our NF-SRG model,

$$\frac{l_{ij}}{g_{ij}} = \frac{w l_{ij}}{g_t} + (1-w)\left[\frac{l_{it}}{g_i} + \frac{l_{tj}}{g_j}\right]. \tag{6}$$

Here g_t is the conductance of the throat surface; l_{it} is the distance from the CoM (center of mass) of pore body i to the throat t_{ij} connecting the two pore bodies; l_{tj} is defined analogously; and $l_{ij} = l_{it} + l_{tj}$. The channel conductance is effective over the length $w\,l_{ij}$. The conductance of pore body i is therefore effective over length $(1-w)l_{it}$; similarly for the conductance of pore body j. The parameter w provides uniform control over the fraction of the pore-to-pore length ascribed to the channel. The end point value, $w = 1$, assumes the pore-to-pore conductance is completely controlled by the throat; $w = 0$ assumes the two pore bodies control the conductance.

The conductances in (4) or (6) are typically modeled on geometric simplifications of the cross sectional shape of pore bodies and throats. For ellipses, regular polygons and arbitrary triangles, the dimensionless conductance $\tilde{g} \equiv g\mu/A^2$ is monotonically related [66] to the dimensionless shape factor $G \equiv A/P^2$ [54]. Here μ is the viscosity of the fluid being transported; A and P are respectively the area and perimeter of the cross section. For arbitrary triangles the relationship between $\tilde{g}$ and G is numerically determined and is shown [62] to be reasonably approximated by the linear relationship,

$$\tilde{g}_T = 0.6\,G, \qquad 0 \le G \le G_{T,\max} = \sqrt{3}/36, \tag{7}$$

where $G_{T,\max}$ is the shape factor for an equilateral triangle. The analogous

34

relationship for rectangles and ellipses is known analytically [65, 66]. Polynomial fits to these analytic relationships are quoted in [66]. For rectangles, the fit is

$$
\begin{aligned}
\tilde{g} &= \tilde{g}_{\max}\left(0.6109\tilde{G} + 0.0630\tilde{G}^2 + 0.3214\tilde{G}^3\right), \\
\tilde{g}_{\max} &= 0.5623/16, \qquad \tilde{G} \equiv 16G, \qquad 0 \le G \le G_{R,\max} = 1/16,
\end{aligned}
\tag{8}
$$

and for ellipses,

$$
\begin{aligned}
\tilde{g} &= \tilde{g}_{\max}\left(0.8077\tilde{G} + 0.0556\tilde{G}^2 + 0.1366\tilde{G}^3\right), \\
\tilde{g}_{\max} &= 1/8\pi, \qquad \tilde{G} \equiv 4\pi G, \qquad 0 \le G \le G_{E,\max} = 1/4\pi.
\end{aligned}
\tag{9}
$$

In (8) and (9), $\tilde{G} \equiv G/G_{\max}$ is the normalized shape factor; $G_{R,\max}$ and $G_{E,\max}$ are, respectively, the shape factors for squares and circles. In both cases, the fits suggest a linear relationship with a correction that is predominantly cubic. Consequently, the relationships for rectangles and ellipses can be approximated by the linear relationships

$$
\tilde{g}_S \;=\; 0.5623\,G, \tag{10}
$$

$$
\tilde{g}_C \;=\; 0.5\,G, \tag{11}
$$

respectively, which, in fact, represent end point linear fits to (8) and (9). These $\tilde{g}(G)$ relationships are plotted in Fig. 11.

Use of the linear relationship (7) underestimates the relationship for arbitrary triangles by as much as 19%. Use of (10) and (11) tend to overestimate conductance compared to that for arbitrary rectangles and ellipses by as much as 33% and 13%, respectively. However, we shall see that these differences are not sufficient to explain differences between the NR-SRG computations and pore-to-pore conductances estimated for the sandstone samples.

When rock data is available (e.g. from XCT images) the shape factors for pore bodies and channels must be determined. The shape factor for a pore body can be determined, for example, as an average over (a sample

35
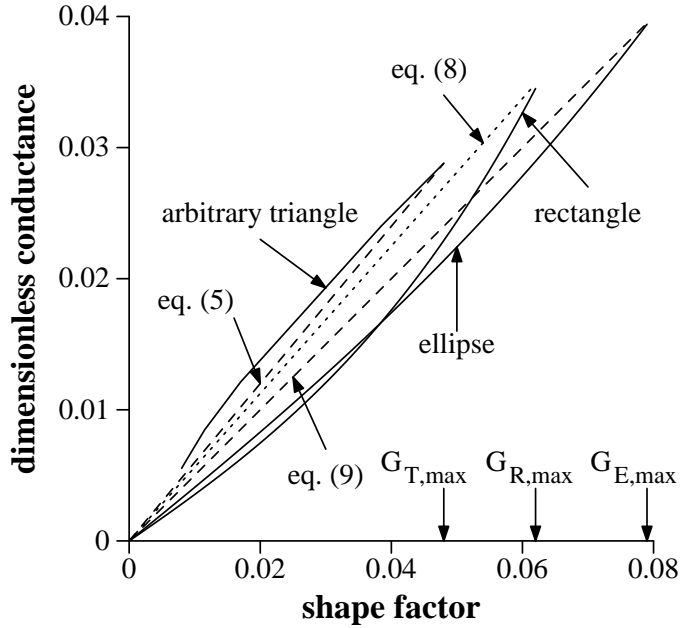
Figure 11: Dimensionless conductance versus shape factor relationships for several geometries.

of) measured cross sections [62, 65] from that pore. As such measures are computationally expensive and direction dependent, in this paper we estimate the shape factor for a pore body by

$$G = \frac{V d_{\max}}{S^2}, \tag{12}$$

where V, S and $d_{\max}$ are, respectively, the volume, surface area and maximum principle diameter for the pore body. Equation (12) is exact for cylinders of constant cross section and length $d_{\max}$. Inherent in the use of (12) for network flow models is that all pore bodies drain along their long axis, which is, of course, an approximation. We estimate the shape factor for a channel directly from its identified throat.

Computation of the conductance for the network element (pore body or throat) is then achieved by assuming that the cross sectional shape is best

36

Table 1: Number of throats and pore bodies in each NF-SRG model and percent of each element (pore, throat) of each shape type as identified according to measured shape factor. tri ≡ triangle; rect ≡ rectangle.

porosity (%)	throats	% throats modeled as:			pore bodies	% pores modeled as:		
		tri	rect	circle		tri	rect	circle
7.5	4,777	47.9	51.8	0.3	3,443	94.3	4.7	1.0
13	10,568	48.2	51.4	0.4	5,741	97.6	2.0	0.4
18	12,787	52.3	47.5	0.2	6,355	97.3	2.0	0.7
22	21,175	51.8	48.0	0.2	10,052	96.2	3.0	0.8

described as either trianglular, rectangular or elliptical [62, 65], specifically:

$$
\tilde{g} = \begin{cases}
0.6\,G, & 0 \leq G \leq G_{T,\max}, \\
0.5623\,G, & G_{T,\max} < G \leq G_{R,\max}, \\
0.5\,G, & G_{R,\max} < G \leq G_{E,\max}, \\
0.5\,G_{E,\max}, & G_{E,\max} < G.
\end{cases}
\tag{13}
$$

In general, all three shapes are needed since each shape has a maximum shape factor. Note that the last case in (13) deals with the possbility that measured shape factors in the data exceed the maximum possible for an ellipse. For the Fontainebleau data set, this occurred in fewer than 0.09% of the cases.

Table 1 summarizes the number of throats and pore bodies determined in each Fontainebleau network model and the percent of each element of each shape type as assigned by measured shape factor under this model.

3.2 Lattice-Boltzmann method and simulation of fluid flow through a channel

3DMA-Rock has the capability of simulating single phase flow via the Lattice Boltzmann-Bhatagnar-Gross-Krook (LBGK) and multiple-relaxation-time (MRT) models. To calculate throat permeabilities, LBGK compressible model with curved boundary conditions [57, 58] and a relaxation parameter of

37

a)   b)
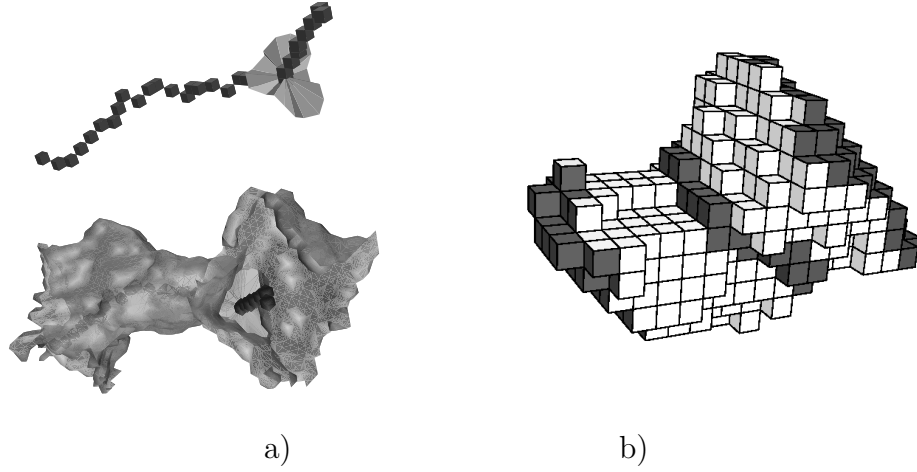
Figure 12: a) A medial axis path showing the computed surface (top). The channel throat surface (bottom). b) A digitized pore space within a distance of 6 voxels on each side. Inlet, outlet and throat barrier are shaded dark gray. Surface voxels are not included. M. Prodanovic *et al.*

$\lambda = 0.75$ was used. Throat permeabilities were computed using the single phase, 3D Lattice Boltzmann model [26, 83]

$$f_i(\vec{x} + \vec{e_i}\triangle t, t + \triangle t) - f_i(\vec{x}, t) = \frac{1}{\tau}[f_i^{eq}(\rho(\vec{x}, t), \vec{u}(\vec{x}, \rho, t)) - f_i(\vec{x}, t)] - 3\frac{w_i}{c^2}\triangle t\vec{e_i} * \nabla p$$
$$(14)$$

The equilibrium distribution function is as follows

$$f_i^{eq}(\rho, \vec{u}) = \rho w_i[1 + \frac{3}{c^2}\vec{e_i} * \vec{u} + \frac{9}{c^4}(\vec{e_i} * \vec{u})^2 - \frac{3}{2c^2}\vec{u} * \vec{u}]. \qquad (15)$$

To implement an external pressure gradient ∇p, [90] introduced a body force, the second term on the RHS of 15, whereas the first term is the single relaxation time scale collision term. This collision term tends to redistribute

38

f_i's closer to the equilibrium, while the second external body force term makes f_i's increase in the direction of the force (and decrease in directions opposite to ∇p).

It is important to remember here that our division of the pore space is into pores separated by triangulated throat surfaces and is not a division into pores separated by channels. We know of no geometrical measure to decide where a pore ends and a connecting channel begins in real rock void space. As a part of LB simulation, there is an important aspect of defining a channel: identifying and reconstructing the throat itself. 3DMA-Rock has such throat algorithms which perform searches along medial axis for the minimal cross sectional surface [46, 91]. Fig. 12 shows the (digitized) medial axis going through the triangulated throat surface, and the channel grain surface. The grain surface is represented by means of the marching cubes algorithm [6, 85]. A channel pore space of 6 voxels on each side of a throat barrier was computed using a 6-connected grassfire algorithm (see Fig. 12). It is found optimal to choose a 6 voxel distance on each side based on the idea that LB simulation is a good approximation to the Navier-Stokes equation.

The 3D, 19 velocity model D3Q19 was used. The values for the weights w_i are $\frac{1}{3}$ for the (0,0,0) direction, $\frac{1}{18}$ for the (1,0,0) (and similar) directions, and $\frac{1}{36}$ for the (1,1,0) (and similar) directions (see Fig. 13).

The single-particle distribution function $f_i(\vec{x} + \vec{e_i}\triangle t)$ at each lattice site $\vec{x}$ is equal to the expected number of identical particles at that site and time t moving along vector $\vec{e_i}$. Thus, nineteen valves, $f_i(\vec{x})$, $i = 0 \rightarrow 18$ represent the particle distribution functions at site $\vec{x}$. A time increment $\triangle t$ of $1.92*10^{-9}$ s was determined from the relation $c = \triangle x/\triangle t$ where $\triangle x$=4.93 μm is the digitized inter-node length and $c = c_s\sqrt{3}$ is the lattice speed, related to the sound speed for water by $c_s = 1482$ m/s. During each time increment, particles move along one of the specified directions $\vec{e_i}$ to the nearest site and collide there

39
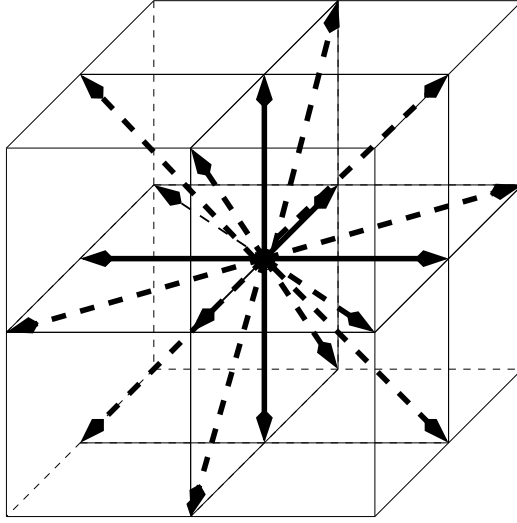
Figure 13: The errows indicate the magnitude and directions of the allowed velocities e_i at a lattice site with a cubic lattice structure in the 3DQ19 model.

with other particles. The collision outcome is the particle distribution function at the new site derived from the Boltzmann equation. Particle state i is defined by a particle velocity $\overrightarrow{u}$, which equals the distance traveled divided by $\triangle t$, so that the model has three different magnitudes of velocity: zero when a particle is at rest, $\frac{1}{2}$c for a particle moving to the closest site, and $\frac{\sqrt{3}}{2}$c for a particle moving to the longest site.

During a collision step, each distribution function is updated toward an equilibrium distribution f_i^{eq} at the rate of $\frac{1}{\tau}$, where τ is the relaxation parameter and is chosen to produce the kinematic fluid viscosity $\nu = \frac{(2\tau-1)}{6}c^2\triangle t$. The kinematic viscosity of water at room temperature and atmospheric pressure is $10^{-6}m^2/s$, requiring a value of τ=0.500237. To achieve convergence computation must be performed with τ in the range [0.525, 1.2], giving an effective kinematic viscosity of water in the range of $[1 \times 10^{-4}, 3 \times 10^{-3}]$.
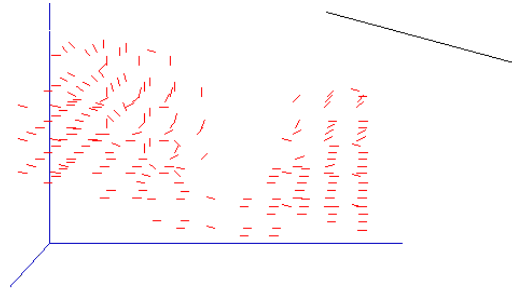
Figure 14: The local directions of velocity vectors determined via smooth fits to the medial axis.

We are interested in permeabilities at steady state flow conditions, which are achieved when the relative velocities at each node satisfies the condition with $\epsilon = 10^{-6}$

$$\frac{\|\vec{u}(x, t + \triangle t) - \overrightarrow{u}(x, t)\|_2}{\|\overrightarrow{u}(x, t)\|_2} < \epsilon. \tag{16}$$

Curved boundary scheme of [57, 58] is used for no-slip boundary condition, which provided improved convergence to steady state flow conditions comparing to standard bounce-back boundary conditions.

For inlet/outlet boundary conditions we require $\partial \overrightarrow{u}/\partial \hat{n} = 0$, where $\hat{n}$ denotes the unit vector in the direction of pressure gradient. Implementation of this boundary condition is then obtained by copying values of appropriate f_i across the boundary. Since the inlet/outlet surface is not planar, see Fig. 12, it is not always possible to find an appropriate neighbor to copy values from, and those nodes are left at temporary equilibrium values. The one interesting implementation detail of the LB computation in a channel is related to the imposition of the pressure gradient. The pressure gradient was modeled in a standard way via an imposed body force. Since pore channels curve, the direction of the body force also curved to follow the channel shape. The local direction was determined via smooth fits to the medial axis of the channel.

41
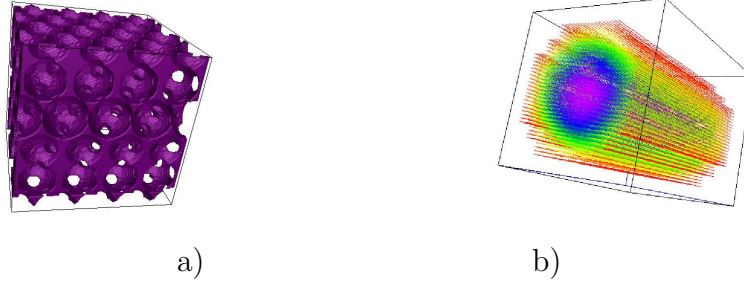
Figure 15: (a) A sealed $130 \times 130 \times 128$ core sample with hexagonal close packing of spheres with diameter of 32 voxels. (b) Hagen-Poiselle flow simulation through the tube.

Boundary conditions should be applied with caution since in practice it is shown that permeability not only depends on the structure of the medium but it also can be strongly effected by boundary conditions imposed on a local flow equations.

The Lattice-Boltzmann method was validated on Hagen-Poiselle flow simulations(flow down cylinders of constant cross-sectional area) see Figure 15. The parabolic radial velocity profiles obtained were in good agreement with analytic values.

3.3 Hydraulic conductance based on Lattice-Boltzmann conductance: the NF-LBC and NF-LBG models

As an alternative to SR approaches, we utilize LB computations to provide an estimate of the effective conductance for each channel. Since the LB method can compute flow through the complex shape of each channel, ideally it should provide an accurate estimation of single fluid conductance for each channel *in*

isolation. By "in isolation" we do not mean performing a LB computation for the fully interconnected network, but rather we mean performing a - highly parallelizable - series of local, separate LB computations, one per channel. In Prodanovic *et al.* [71], we introduced such computations for each throat region (channel), as identified by 3DMA-Rock analysis of an XCT image of a Berea core. Here, we apply this method to the four Fontainebleau images and utilize the conductances directly in a network flow model.

As there are thousands of throat regions in each image, the LB computation has to be robust, automated and inexpensive. Intuitively, the channel should be defined from the CoM of one pore body through to the CoM of a connected neighbor. However, the potential increase in complexity of the geometry of the channel as one moves away from the throat and enters a pore body, especially if the body has coordination number greater than two, leads to robustness issues in the LB computation in implementing boundary conditions (input, output and side). To minimize potential geometrical complexity and to reduce CPU time, the computations in Prodanovic *et al.*[71] captured the digitized channel shape enclosing the pathway to an effective distance of 37 μm on each side of the throat surface. We use the same restriction in our computations, thus computing the conductance for the channel over a distance of 74 μm (or a shorter distance if the CoM to CoM pore-to-pore distance is shorter). In addition to enhancing robustness and speed of the LB computations, this restriction recognizes that the conductance of the channel for single phase, incompressible flow, is dominated by the throat region.

For each separate sandstone, Fig. 16 summarizes the LB computations of the dimensionless conductance computed for each pore-to-pore connection as a function of the shape factor of the throat in that channel. Also shown on each plot is the dimensionless conductance computed by the shape factor model (13). Consistent with this model, the LB conductances reveal a trend of

43
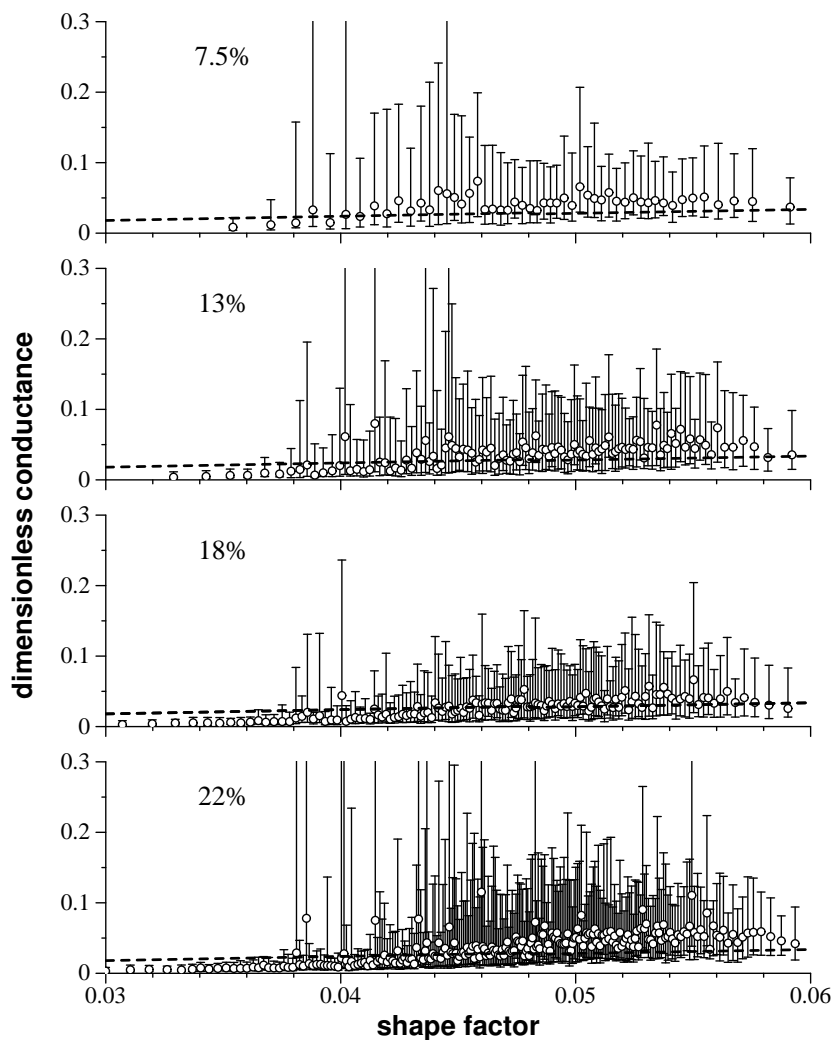
Figure 16: First to third quartile ranges of dimensionless conductances for individual pore-to-pore connections as computed by the LB method, binned by value of the shape factor for the throat in the channel. Bin sizes are adjusted so that each bin contains data on 100 connections. Median (second quartile) values are indicated by open circles. The dashed line is the prediction based upon the shape factor models (7), (10) and (11). Only data in the range $0.03 \leq G \leq 0.06$ is shown; a minor amount of data exists in the range $[0.06, 0.08]$.

Table 2: Best fit parameter values to the form $\tilde{g} = \tilde{g}_1 G^p$ for the data in Fig. 18.

porosity	$\tilde{g}_1$	p
7.5	65.5	2.45
13	7,240	4.04
18	7,990	4.15
22	27,400	4.47

increasing $\tilde{g}$ with shape factor. The variances in the LB conductances are large, but the trend of the median values shows a greater rise than that predicted by (13). Typically the shape factor model (13) overestimates fluid conductance for small shape factors and underestimates fluid conductance for large shape factors.

Least-square fits of the form

$$\tilde{g} = \tilde{g}_1 G^p \tag{17}$$

to the median values of the LB-computed conductance versus shape factor are shown in Fig. 18. Values of the parameters determined from the fits are given in Table 2.

Except for the 7.5% data set in which the variability of the data precludes a decent fit to the form (17), the fits indicate that the power law with $p \sim$ 4.2 would provide a reasonable analytic form for generating representative dimensionless conductances for the channels in Fontainebleau sandstone. The lack of fit for the 7.5% porosity data may be explainable by the observation [12] that, as soon as porosity is small enough, the average pore entry radius gets smaller and pore entry radii are not well sorted, producing greater microscopic heterogeneity.

Fig. 17 compares the $\tilde{g}(G)$ fits to the data in Fig. 18 with the relationships predicted by the triangle, rectangle and ellipsoidal geometry models. These geometric models do not capture the more rapid rise of observed conductance as the shape factor increases. In our view, this reflects the observation [45]
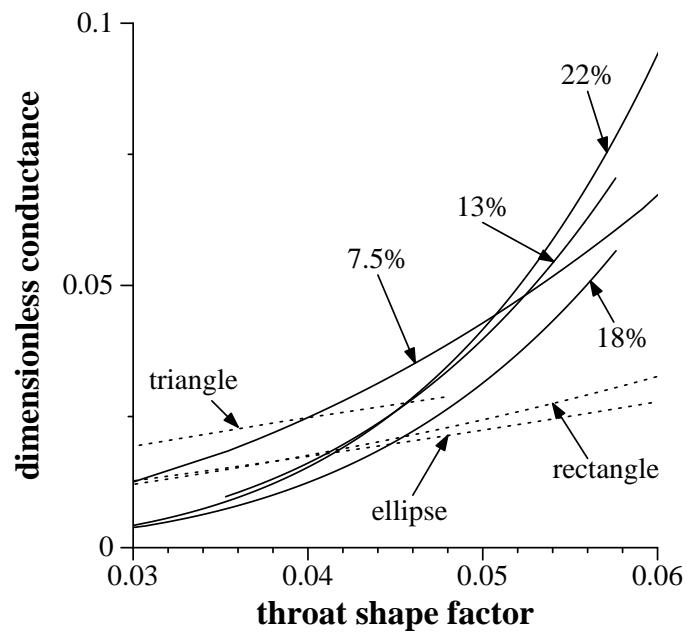
Figure 17: Comparison of fits to dimensionless conductivity versus throat shape factor based upon LB computations for pore-to-pore connections in Fontainebleau sandstones with the analogous relationships for triangle, rectangle and ellipsoidal geometries.
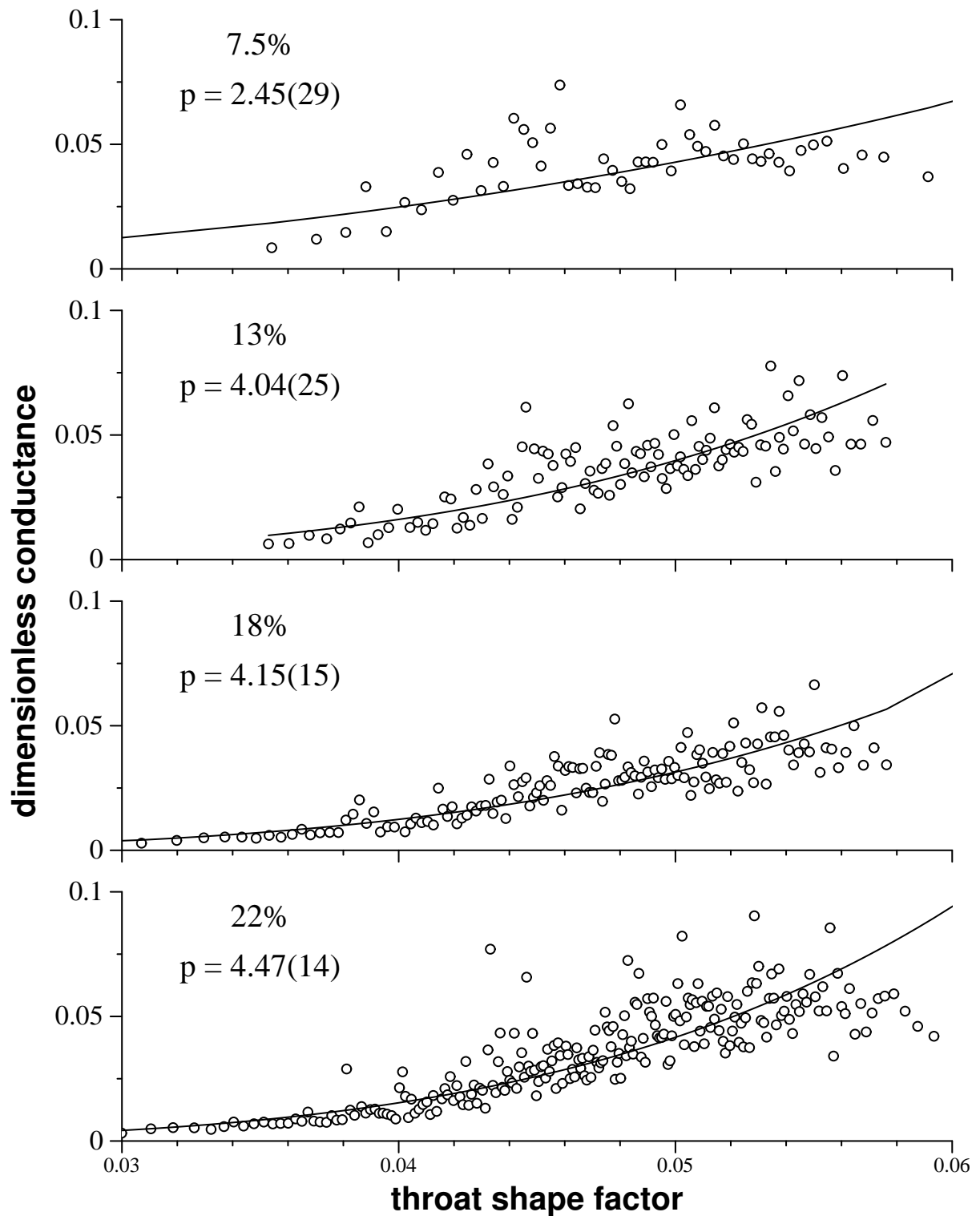
Figure 18: Least-squares fit (solid curve) of the form $\tilde{g} \sim G^p$ to the median values (open circles) of the data in Fig. 16. Only data in the range $0.03 \leq G \leq 0.06$ is shown; a minor amount of data exists in the range $[0.06, 0.08]$.

these geometrical models do not adequately match cross sectional shapes in Fontainebleau sandstones.

For each rock sample, a network flow model (NF-LBC) was created in which the conductance computed for each channel by the LB method was used directly in (3). In approximately 3% of the computations, the LB computation for a channel returned a negative conductance, indicating that net flow opposed the direction of the pressure gradient. This 3% of the data was not, of course, included in Fig. 16.

Examination of cases in which this occurred showed circulation currents resulting from geometrical complexity of the channel in relation to imposed input/output boundaries. In such cases, a dimensionless conductance for the channel was selected from Fig. 16. Rather than using the analytic form (17), a random conductance value was chosen from the statistical distribution of conductances computed for the bin appropriate to the shape factor measured for the throat.

A second network flow model (NF-LBG) was created in which only the analytic form (17), with the porosity-appropriate fitting parameters taken from Table 2, was used to compute the pore-to-pore conductance, with the shape factor, G, determined from the throat connecting the two pores.

3.4 Bulk permeability prediction

The NF-SRG, NF-LBC, and NF-LBG models described in §3.1 and §3.3 were used to compute bulk permeabilities (in the $x-$, $y-$, and $z-$directions) for each of the four sandstone networks. The computation for the pore-to-pore conductances has been discussed; the other details of the single phase, incompressible flow models are standard:

- constant pore pressures are imposed at inlet/outlet sides, no-flow conditions exist at the remaining four sides of each cube;

- conservation of volumetric flow through each pore body leads to a system of linear equations yielding interior pore pressures; Volume conservation of fluid flow implies that volumetric in-flow rate equals out-flow rate in every pore;

$$\sum q_{AK} = \sum \frac{g_{AK}}{l_{AK}}(P_A - P_K) = 0, \tag{18}$$

where we sum over all pores K connected to pore A.

Regrouping the RHS of 3.4 gives

$$P_A\left(\frac{g_{A1}}{l_{A1}} + \frac{g_{A2}}{l_{A2}} + ... + \frac{g_{AK}}{l_{AK}}\right) - \left(P_1\frac{g_{A1}}{l_{A1}} + P_2\frac{g_{A2}}{l_{A2}} + ... + P_K\frac{g_{AK}}{l_{AK}}\right) = 0, \tag{19}$$

Applying the conservation law to each pore yields a system of equations with the number of unknown pressures equal to number of interior pores. The RHS of the below system of equations is formed by imposing pressures on the inlet and outlet boundaries. Coefficient matrix of this system is symmetric;

$$\begin{pmatrix} \left(\frac{g_{1I}}{l_{1I}} + ... + \frac{g_{1J}}{l_{1J}}\right) & 0 & ... & -\frac{g_{1J}}{l_{1J}} & 0 \\ -\frac{g_{2I}}{l_{2I}} & \left(\frac{g_{2I}}{l_{2I}} + ... + \frac{g_{2J}}{l_{2J}}\right) & 0 & ... & -\frac{g_{2J}}{l_{2J}} \\ \vdots & \vdots & \ddots & \vdots & \vdots \\ -\frac{g_{NI}}{l_{NI}} & ... & -\frac{g_{NJ}}{l_{NJ}} & 0 & \frac{g_{NI}}{l_{NI}} + ... + \frac{g_{NJ}}{l_{NJ}}) \end{pmatrix} \begin{pmatrix} P_1 \\ P_2 \\ \vdots \\ P_N \end{pmatrix} =$$

$$
\begin{pmatrix}
0 \\
\frac{g_{2K}}{l_{2K}} P_K^{inlet} \\
\vdots \\
\frac{g_{NT}}{l_{NT}} P_T^{outlet}
\end{pmatrix}.
$$

(Note, here, pore 2 is connected to the inlet pore K and pore N is connected to the outlet pore T)

- the pressure system is solved by a preconditioned conjugate gradient method;

- the total flow rate, Q, at the outlet is obtained and Darcy's law,

$$
Q = \frac{KA}{\mu} \frac{(p_{in} - p_{out})}{L},
\tag{20}
$$

is applied to compute an absolute permeability K for the core having outlet cross sectional area A and brine viscosity $\mu = 1.06$ cp.

Darcy's law was introduced originally as an empirical relationship based on experiments on steady state flow in a vertical homogeneous sand filter and 20

Table 3 presents the computed permeabilities; for the NF-SRG model permeabilities for three values of w are presented. The $x-$, $y-$ and $z-$ permeabilities are quite similar, with the relative difference between directional permeabilities decreasing with porosity.

We note that the CPU time needed to perform the necessary LB computations for conductances in each channel and then execute the resultant NF-LBC model is still cheaper (both in memory and CPU time) than employing LB computation alone to compute the bulk permeability on any of the digitized Fontainebleau samples. The LB computations for conductance of each individual channel have the additional advantage that they are perfectly parallizable; different processors handling the computations for different channels.
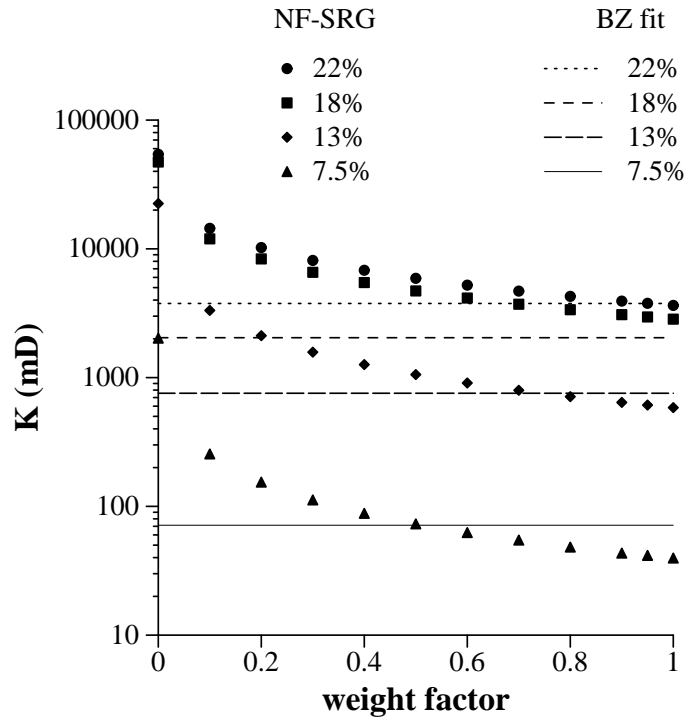
Figure 19: Dependence on the series conductance weight factor (w) of the (direction averaged) absolute permeability computed for each of the four Fontainebleau image samples by the NF-SRG model of §3.1. The solid lines represents the absolute permeability predicted for each porosity value as determined by the analytic best fit to the experimental data of Bourbie and Zinszner (BZ) [12].

Table 3: Comparison between calculations of directional bulk absolute permeability: K_w - NF-SRG model; K_{LBC} - NF-LBC model; K_{LBG} - NF-LBG model.

porosity (%)	direction	K_w (mD), $w =$			K_{LBC} (mD)	K_{LBG} (mD)
		1.0	0.7	0.0		
7.5	x	40.12	54.53	1573	43.5	55.18
	y	49.76	68.89	2623	62.1	71.73
	z	29.23	40.79	1879	43.0	42.58
13	x	619	841	23582	686	775
	y	541	741	21916	664	687
	z	596	811	21922	692	753
18	x	2976	3872	46463	2236	2494
	y	2808	3667	48368	2158	2355
	z	2750	3604	46912	2220	2394
22	x	3505	4544	5411	4060	3761
	y	3668	4721	5330	3830	3994
	z	3737	4828	5520	3871	3982

In Fig. 19 we explore the dependence on choice of w for the SR computation of absolute permeability in the four Fontainebleau network models. The absolute permeability is displayed as the average of bulk permeabilities computed for flows in the $x-$, $y-$ and $z-$directions. As we do not have permeability measurements available from our core samples (which were imaged dry), these network flow computations are compared against the Kozeny-Carman type analytic fits,

$$K_{BZ} = \begin{cases} 2.75 \cdot 10^{-5} \ \phi^{7.33} & \text{for} \quad \phi < 9, \\ 0.303 \ \phi^{3.05} & \text{for} \quad \phi \geq 9, \end{cases} \tag{21}$$

obtained from the rather extensive experimental permeability-porosity data measured in the classic work by Bourbie and Zinszner [12]. As w is varied, the computed value of permeability varies typically by an order of magnitude. Depending on porosity, the choice of w producing best fit between the network model and the data of Bourbie and Zinszner varies from $w \sim 0.5$ at 7.5% porosity to $w \geq 0.9$ at 22% porosity. This rising dependence of w with porosity

makes qualitative sense, the effect of throats on permeability becomes more important as porosity rises.

Note that, for all values of w, the bulk permeability computed for the 18% porosity Fontainebleau NF-SRG model disagrees with the Bourbie and Zinszner experimental value (of 2040 mD). This discrepancy is interesting, as the 18% NF-LBC model (see below) is in good agreement with the Bourbie-Zinszner value. This would indicate that there are conditions in which the geometry of the channel cannot be adequately captured by the series resistance type models. Similar limitations of computations from geometrical-based models relative to LB simulations have been reported recently [25].

The results in Fig. 19 imply that use of the model (6) for network computations based upon SR computation for general rock models would require either an average choice for the weight factor (e.g. $w = 0.7$), or adoption of a schedule for modifying w with porosity based upon parameter fitting studies. Our main point here is that these strategies are either explicitly or implicitly ad hoc and produce results that are sensitive (note the logarithmic nature of the y-axis in Fig. 19) to the chosen strategy. The reliance of NF-SRG type models on the dimensionless shape factor, which captures only a simplified description of the pore geometry, results in "tuned" NF models that work best over a limited range of porosity. See [15] for a similar conclusion.

Fig. 20 compares results from the NF-SRG, NF-LBC, and NF-LBG computations with the Bourbie-Zinszner analytic model. The dependence of the NF-SRG model on the parameter w is summarized by elucidating the entire range of permeability values generated as w is varied. The NF-LBC computations follow the Bourbie-Zinszner analytic model very well. Table 4 quantifies the relative error between the network flow model results and the Bourbie-Zinszner analytic fit. Only results from three values of w are included in Table 4. Except for the lowest permeability, the relative error in the NF-LBC
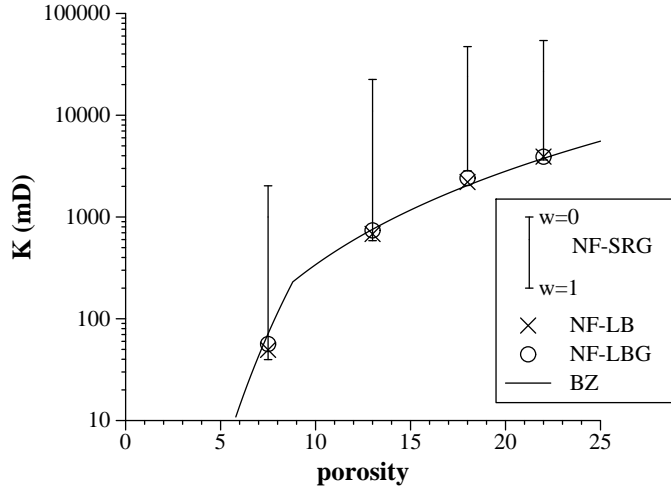
Figure 20: Comparison of the direction averaged, bulk absolute permeability computed for each of the four Fontainebleau image samples by the NF-SRG, NF-LBC, and NF-LBG models of §3.1 and §3.3. BZ: Analytic fit to Bourbie-Zinszner data.

Table 4: Comparison between calculations of average bulk absolute permeability: K_w - NF-SRG model (§3.1); K_{LBC} - NF-LBC model (§3.3); K_{LBG} - NF-LBG model (§3.3); K_{BZ} - analytic fit to experimental data of Bourbie and Zinszner [12]; e_α - relative agreement between numerical computation and experimental data, $e_\alpha \equiv (|K_\alpha - K_{BZ}|/K_{BZ})$ where $\alpha = w$, LBC, LBG.

porosity	K_{BZ}	K_w (mD), $w =$			K_{LBC}	K_{LBG}	e_w, $w =$			e_{LBC}	e_{LBG}
(%)	(mD)	1.0	0.7	0.0	(mD)	(mD)	1.0	0.7	0.0		
7.5	71.4	39.7	54.7	2030	49.5	56.5	0.44	0.23	27.4	0.31	0.21
13	756	585	798	22500	681	739	0.22	0.055	19.7	0.10	0.02
18	2410	2840	3714	47200	2205	2414	0.18	0.54	18.5	0.085	0.0016
22	3760	3640	4700	54200	3920	3910	0.032	0.25	13.4	0.042	0.04

models is 10% or lower.

Our sensitivity study indicates that network flow models utilizing series resistance computations for pore-to-pore conductance are capable of "tuning" bulk absolute permeability values over at least one order-of-magnitude. Our results show that a "tuned" model will produce sharp bulk values only over a limited range of porosity.

By comparing with Lattice Boltzmann computations, our results indicate that network flow models employing channel conductances based upon shape factor do not capture a sufficiently rapid increase of conductance with increasing shape factor. We have extracted a power law model appropriate for Fontainebleau sandstones which, more accurately, captures this trend.

The NF-LBC hybrid network flow - Lattice Boltzmann model that we have introduced encorporates advantages of both methods. The Lattice Boltzmann simulations are run locally, and in a highly parallelizable fashion, to provide pore-to-pore conductances for input into a network flow model. This hybrid model eliminates the need for series resistance conductance computations, and utilizes the superior ability of the Lattice Boltzmann simulations to capture individual channel geometry.

The modified NF-LBG model, which requires only estimates for throat shape factors and the two parameters appearing in (17), should enable more accurate computations in "artificial" medium models, i.e. those not based upon a specific 3D realization.

Chapter 4

Multi-phase pore networks

Multiphase flow through rocks is far less understood than single-phase flow. The last decade has seen increased interest in the usage of pore-scale networks for studies of a wide range of phenomena. The most common use is to predict relative permeability and capillary pressure as a function of water saturation. A precise knowledge of the relative permeability coefficients of porous media is of critical interest to environmental science and techniques. It forms an unavoidable step in modeling chemical or radioactive-type transfers enabling a safety coefficients to be defined in relation to confinement structures [18]. Through this understanding, many questions can be addressed: Can a change of injected brine salinity increase oil recovery and by how much? Can relative permeability be changed by introducing water-based gels [65]? How can we limit oil-trapping?

Using Fontainebleau sandstone samples varying from 7.5% to 22% porosity, and pore networks there of provided by 3DMA-Rock, our goals in this chapter are:

1. calculate capillary pressure/saturation and relative permeability curves under primary drainage;

2. understand the relative importance of the geometrical parameters of Fontainebleau sandstone with different porosities in determining flow behavior;

3. determine the accuracy of the computations by comparison with experimental results;

4.1 Displacement mechanisms and two-phase flow properties

For two-phase flow description we need to define some terminology. For a given substrate, each pair of fluid phases in contact with each orther and the substrate, have relative surface wetting ability which can be quantified in terms of a contact angle θ (Fig. 21). The fluid having angle in the range $0° < \theta < 90°$ is called the wetting fluid, the other is referred to as non-wetting. In Fig. 21, σ_{SA} and σ_{SB} are the surface tensions between the solid and fluids A and B respectively, while σ_{AB} is the interfacial tension between the two liquids. In equilibrium, all three surface tensions are related by the Young equation:

$$\sigma_{AB} \cos \theta = \sigma_{SA} - \sigma_{SB}. \qquad (22)$$

When the three phase contact line is not in the equilibrium, the displacement of one liquid by the other is observed. When the meniscus movement displaces the non-wetting fluid, the flow is said to be imbibition and θ is referred to as the advancing angle (Fig. 21(b, right)). When the meniscus movement displaces the wetting fluid, the flow is referred to as drainage and θ is referred to as the receding angle (Fig. 21 (b, left)). A system may go through repeated cycles of imbibition and drainage (e.g. soils under periodic precipitation events). We are interested in primary drainage, when a
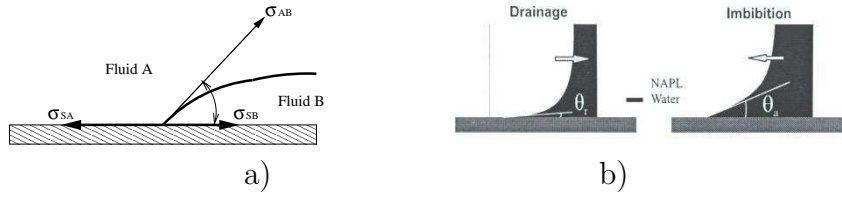
Figure 21: (a) Equilibrium at a line contact forms a fixed contact angle θ. The depicted angle of contact is between two boundaries: fluid B/solid and fluid A/fluid B. Here liquid B is the wetting, liquid A is the non-wetting.

non-wetting, non-aqueous phase liquids (NAPL) migrates into a completely water-filled core. For drainage experimental evidence indicates that we need to consider only one displacement mechanism, referred to as piston-type displacement. Our goal is to simulate primary drainage by applying this displacement process and to calculate the relative permeability of the system and the capillary pressure-saturation relation governing the system.

In the current study we will use values of absolute permeabilities computed via LB-based models but implement an NF-SRG model to calculate the parametric relationships (capillary pressure-saturation, relative permeability-saturation) that are required for continuum-scale description of multiphase flow. NF-SRG model allows to make easy estimation of both phase pore saturations by simplifying pores with appropriate constant cross-sectional tubes. wo-phase primary drainage is simulated in four different porosity Fontainebleau samples. We assure immiscible, incompressible, creeping Newtonian flow fluids. The injected fluid is a non-wetting oil with viscosity 1.40 cp and 0.76 g/cm^3 density, while the in-situ fluid is brine with viscosity 1.06 cp and density 1.02 g/cm^3. Oil-brine interfacial tension is 35.0 mN/m. The separate flow rates at the wetting (v_1) and non-wetting (v_2) fluids are given by the coupled

Darcy equations:

$$v_1 = -\frac{k_{11}}{\mu_1} \triangledown P_1 - \frac{k_{12}}{\mu_2} \triangledown P_2, \qquad (23)$$

$$v_2 = -\frac{k_{21}}{\mu_1} \triangledown P_1 - \frac{k_{22}}{\mu_2} \triangledown P_2. \qquad (24)$$

Here P_i is the pressure in fluid i. Fluid i moves both from the gradient of pressure on itself as well as the gradient of pressure in the other fluid. The proportionality constants k_{ij}, k_{ii} are referred to as effective permeabilities. The ratios k_{ij}/μ_i and k_{ii}/μ_i are called mobilities. The proportionality coefficients k_{ij} depend on the boundary condition at the interface between the two phases. In our study we assume that capillary forces control the process (the capillary number $\mu_i q_i/\sigma$ (i=1,2) is low, eg., less than about 10^{-6}) and viscous forces ($\mu_{nw}/\mu_w > 1$) are negligeable. There is therefore no hydraulic slip at fluid-fluid interfaces, which creates a lubricating effect, and the coupling coefficients $k_{12}=k_{21}=0$. Under this assumptions, (23) and (24) uncouple and only the effective phase permeabilities k_{ii} play a role in the Darcy system. Equations (23) and (24) reduce to the uncoupled form of Darcy's law for two-phase flow:

$$Q_i = (\frac{k_i A}{\mu_i})\frac{\Delta P_i}{L}, (i = 1, 2), \qquad (25)$$

where $Q_i = q_i A$ is a bulk volumetric flow rate, ΔP_i is the pressure drop across the system, μ_i is the viscosity of fluid i, A is the cross-sectional area of the sample and L is its length in the direction of the pressure drop. K_{ii} is replaced with notationally simpler k_i and is the effective permeability of phase i. The relative permeability for fluid i is defined as the ratio $k_{ri}=k_i/k$ where k is absolute permeability of the system. In general though, the assumption of negligeable viscous forces is incorrect and there is a viscous coupling between the two phases, which leads to k_{12} and k_{21} not equal to zero (the mobility tensor has off-diagonal terms). At the beginning of primary drainage the sample is fully saturated with water ($S_w=1$). Fontainebleau sandstone is considered to

be strongly water-wet with a receding contact angle of 0 degrees. The fully wetting condition presumes that there is no trapping of non-wetting phase and the connate water saturation will be zero. Consequently the wetting phase will be hydraulically connected throughout the pore network [9]. The result is the existence of two co-current, continuous flows (one for each fluid) which reside side by side in the same pore space. The wetting phase generally flows along pore walls, whereas the non-wetting phase flows in the central part of each pore and surrounded by the wetting phase. Therefore the information is needed on the distribution of the two fluids in each and every pore (i.e. the fraction of the pore cross-section occupied by each fluid must be known at every point) [21].

Large throats (having small entry pressure) are going to be preferentially invaded, then smaller ones come into play. It is important to note that pore entry pressures are therefore completely determined by the size and geometry of its upstream facing the throats. In §4.3 we investigate several ways of estimating pore entry pressures: the first based on Mayer and Stowe and Princen (MS-P) method [67, 68, 69] and the second based on computations of arc meniscus radii at fluid entry [45] for actual throat geometries using Held's VRONI software package [48].

A second necessity in the accurate estimation of relative permeability curves is the calculation of the hydraulic conductance for each fluid simultaneously flowing in a pore. In §4.4, we describe a method introduced by Patzek and Oren [65, 62] for calculation of the hydraulic conductance of each phase and for calculation of phase saturations in a single pore. Both computations require the precise knowledge of where each phase resides in the pore. The complex geometry of real pores necessitates the use of simplified pore shapes which non-the-less capture important features of the angular nature of pores.

Calculation of relative permeability and water saturation is made at each capillary pressure $P_c = P_{nw} - P_w$ (the pressure difference between two phases) for both liquids. The saturation of fluid phase i is defined as

$$S_i = \frac{V_i}{V}, \tag{26}$$

where V_i is volume of fluid phase i in the sample and V is the total pore volume in the sample.

Similar to the absolute permeability system of equations, relative permeability system of equations is constructed, and total flow in each phase is calculated. Then, relative permeabilities are determined from 25. Step by step procedure is described in §4.2.

In §4.5 we present the results of our NF computations, validate them against experimental published data, and try to understand a scope of effect of micro-structure parameters on controlling hydrodynamic behavior in Fontainebleau sandstone and other porous materials.

4.2 The Bond Invasion-Percolation Problem

In two phase flow, the invading fluid must be connected to the inlet to continue invasion and the defending fluid must be connected to the outlet to be displaced. This dynamic percolation is called invasion percolation (IP). In a permeable rock, fluid flow paths are determined by the randomly oriented pore network. The fluid transport in the pore networks can be described as a percolation process [19]. The concept of percolation theory is closely allied with pore network models. Percolation theory provides a mathematical framework to analyze deterministic motions in a random medium [14]. In the case of fluid-fluid displacement in porous media, the deterministic rule is the Laplace equation for capillary displacement rule, while the randomness comes from the random geometry of each throat. Since drainage is controlled by

throats (referred as links and bonds in IP terminology) the drainage is equivalent to bond invasion-percolation process. The mechanisms briefly described below is referred to as "piston-type" drainage and forms the basis for the invasion percolation algorithm. As the applied capillary pressure is gradually increased, penetration continues into the pore until the local minimum pore radius of curvature of the arc-menisci in the corners at the throat is obtained. By equating the radius of curvature of arc meniscus (AM) to the first curvature of the invading interface, the threshold capillary entry-pressure can be found [2]. We calculate all entry pressures for throats, using either equations derived by Mason and Morrow (MS-P method) or using VRONI method and sort them in strictly ascending order. A further increase in capillary pressure will result in non-equilibrium displacement of the wetting liquid, which expands into an adjacent pore and stops when a narrower throat is reached. At this moment the capillary pressure must be increased for further penetration. When all the menisci separating continues fluid phase are found to be stable (that is, they support the imposed capillary pressure), the system has reached a new equilibrium [73].

Therefore a bond-invasion percolation algorithm for primary drainage consists of the following steps:

1. The receding contact angle during primary invasion is assumed to be zero since at the beginning of simulation the pore is completely water-filled and only later, in imbibition process, the contact angle changes but it yet has to be explored;

2. At each capillary pressure level, find all throats not yet invaded that have entry-capillary pressure smaller than the current valve and have at least one adjacent pore filled with non-wetting liquid [2].

3. Invade these throats.

4. Displacement continues (repeat steps 2-3) until all menisci are found to be in equilibrium position.

5. After all possible throats and pores are invaded, calculate water-phase saturation, phase conductances (i=1,2) for each pore in the pore network.

6. Compute relative phase permeabilities at this water-saturation;

7. Increase the capillary pressure to a higher valve and repeat steps 2-5 until some specified maximum capillary entry pressure or minimum water saturation is reached. Since there is an assumption that water filaments can drain completely, the irreducible wetting phase saturation reaches zero value.

We emphasize one more time that relative permeability values of phase i are computed using Darcy's Law:

$$k_{r,i} = \frac{Q_i \mu_i L}{kA \triangle P_i},\qquad(27)$$

where Q_i is the volumetric total flow rate of phase i, μ_i is the phase i viscosity, $\triangle P_i$ is the phase i pressure drop across the network and k is the absolute permeability of Fontainebleau rock sample computed via the NF-LBC model (see §3.3). So at several overall water-phase saturations we solve for the pore (nodal) pressures and then calculate each relative permeability by using 27 for water and non-wetting fluid. The capillary number is sufficiently low, fluid/fluid interfaces are stable (no slipping) and two fluids are in equilibrium, so we have two independent networks (two fluids flows). As mentioned in §4.1 one or the other fluid flow behaves as another fluid phase was replaced by a solid (phase immobilization) therefore the computation of the permeability of each phase is identical to the calculation for a single-phase flow except that each phase is considered to occupy a separate sub-network of the pore space.

Since water remains continuous throughout the network, the pore pressure calculation is applied to all pores except the ones connected to the inlet and outlet faces [2]. We start a calculation of non-wetting relative permeability values when it reaches the bottom. Such state is called a breakthrough point. The inlet face pores are assigned an arbitrary pressure P_{in}, whereas outlet face pores are assigned arbitrary pressure P_{out}.

From the measurements above one can produce capillary pressure curve and relative permeability curves for each phase versus wetting fluid saturations. For drainage these are referred to as primary drainage curves.

If a wetting liquid is at atmospheric pressure, in order to displace this fluid the pressure in an invading non-wetting fluid has to be increased above atmospheric pressure by an amount given by the capillary pressure. The capillary pressure P_c is given by

$$P_c = P_{nw} - P_w = \frac{2\sigma}{R}|cos(\theta + \phi)|, \tag{28}$$

where σ is the surface tension between the two liquids, P_{nw} is the pressure in the non-wetting fluid, P_w is the pressure in the wetting fluid and $r = \frac{R}{|cos(\theta+\phi)|}$ is the mean radius of curvature of the meniscus (see Fig. 4.2, here θ is angle A, and ϕ is angle B). Eq. 29 follows from Laplace's equation

$$P_{nw} - P_w = \frac{2\sigma}{r_m}, \tag{29}$$

where r_m is the mean radius of curvature, maintaining mechanical equilibrium between two fluids. Note that $r_m = \infty$ when $P_{nw} = P_w$ and the meniscus becomes planar.

We consider bond-invasion percolation problem with no trapping. Our system of interest (Fontainebleau sandstone) is strongly water-wet; the wetting fluid tends to spread on the solid surface and a solid tends to imbibe the wetting phase thus forming a wetting layer that is continues network throughout the system. As a result, the wetting fluid can always escape from any location

64
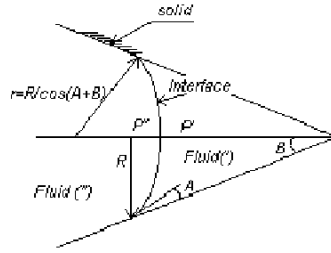
Figure 22: Menisci in a conical capillary.

within the network. During primary drainage the wetting liquid occupies the pore corners, while the non-wetting fluid resides in the middle. As stated, it is assumed that the wetting layer is continues; that is the wetting layers in the corners are connected to those in adjacent pores and throats [8]. Despite this assumption, in reality zero water saturation is very hard to reach, unless the capillary pressure is allowed to become arbitrary large.

4.3   Primary Drainage Pore Entry Pressures

Capillary entry pressure depends on many parameters such as the receding contact angle, θ_i, surface tension and radius of curvature. The invading interface captures complex physical relation between two fluids, fluids and solid and can hold nonzero stresses so that capillary forces prevent non-wetting phase from spontaneously entering wetting fluid filled pores. To move the interface all these relations should be taken into account. In our case, water-wet system, θ_i is equal to zero. We investigate two methods of computing capillary entry pressure P_C^e. Note that at the capillary entry pressure (threshold pressure), non-wetting fluid enters the throat with a fixed curvature and displaces water from the central part of the throat, leaving some of the water as AM's in the corners (see Fig. 23). The drainage of an individual pore in a network depends

in part upon the rest of the pore network. Below are the brief description of three methods used to compute throat entry pressures.

4.3.1   MS-P method

Mason and Morrow [54] applied the MS-P theory to derive a general expression in terms of a throat shape factor, G for the drainage threshold capillary pressure in triangular pores. The key idea is that the MS-P method for calculating threshold capillary pressure relies on equating the meniscus curvature of the arc meniscus (AM's) to the curvature of the invading interface, the main meniscus, referred to as the main terminal meniscus (MTM). This assumption holds in the absence of gravity. The meniscus curvature is $C=1/r_1+1/r_2$, where r_1 and r_2 are the principal radii of the meniscus and are related to the mean radius of curvature r_m as $1/r_m=1/2(1/r_1+1/r_2)$. For a cylindrical or triangular tube, the cap is spherical and r_1 and r_2 are equal ($r_m=r$) and the pressure difference across a curved interface is described by the classical Laplace equation:

$$P_c = \frac{2\gamma_{nw}}{r}. \tag{30}$$

If the AM's were displaced a small distance dx, the work of the displacement must be balanced by the change in surface free energy,

$$P_c A_{eff} dx = (L_{nw}\gamma_{nw} + L_{ns}\gamma_{ns} - L_{ns}\gamma_{ws})dx, \tag{31}$$

where the subscripts s, n and w refer respectively to solid, non-wetting, and wetting phase, A_{eff} is the effective area occupied by non-wetting phase, P_{eff} is the effective perimeter occupied by non-wetting phase, L_{nw} refers to the perimeter of the AM's, L_{ns} refers to the length of the solid wall in contact with non-wetting phase. From Young's equation, $\gamma_{ns} - \gamma_{ws} = \gamma_{nw}cos\theta_r$, $\theta_r = 0$ and eq. 31 simplifies to

$$\frac{P_c}{\gamma_{nw}} = \frac{1}{r} = \frac{L_{nw} + L_{ns}}{A_{eff}} = \frac{L_{eff}}{A_{eff}}. \tag{32}$$

A_{eff} and $L_{eff} = L_{nw} + L_{ns}$ are readily available from elementary triangular geometry. The details of calculation can be found in [62]. The threshold capillary pressure is governed by both the pore shape and the receding contact angle θ_r which is zero in our water-wet system.

$$P_c^e = \gamma_{nw}C = \frac{\gamma_{nw}(1 + 2\sqrt{\pi G})}{r}, \tag{33}$$

where r is the inscribed radius of the throat, G is its shape factor, γ_{nw} is the surface tension between non-wetting and wetting phases, C is a curvature of a meniscus. C is fixed by the boundary conditions of the interface and is therefore governed by both pore structure and wettability. Evident disadvantage of such method that it uses triangular simplified geometry of throats. However, corners of triangular throat resemble its grooves and crevices since they contain water films. In §4.4 we show that triangular presentation of throats simplifies calculations of hydraulic conductances.

4.3.2 VRONI method

Algorithms, and in some cases, complete software packages have been developed to analyze the geometry of the pore structure [1] from Computed Tomography (CT) images [45]. Here we therefore can consider the full polygonal representation of each throat obtained using the 3DMA-rock software package as deduced from the CT images of a suite of four Fontainebleau sandstone core sample discussed in Chap. 2. A detailed discussion of throat finding algorithm can be found in Lindquist and Venkatarangan [46]. In summary, the throats minimize cross sectional area, not planar, by following the cross sectional geometry of the channel. Following the work of Mason and Morrow, we project digitized throats onto a plane that is perpendicular to the average normal to the throat surface. A deviation from planarity is rather mild with no significant artifact. So the basis of computation is similar to MS-P method,
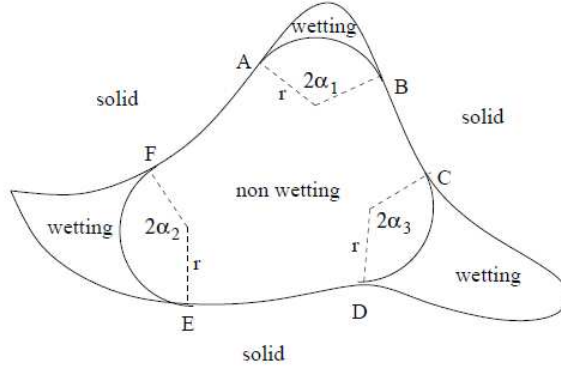
Figure 23: Schematic of non-wetting fluid occupation of the cross section of a capillary tube of arbitrary, simply connected, cross sectional shape. (W. B. Lindquist, 2006)

in fact for each throat a radius of curvature of the arc meniscus at the critical (threshold) entry pressure, r_e, defines the critical entry pressure for that throat

$$P_c^e = \gamma_{nw}/r_e. \tag{34}$$

From Fig. 23 it is seen that

$$L_{nw} = 2r \sum \alpha_i \tag{35}$$

and if substitute 34 and 35 into 29, the resulting quadratic equation is

$$2r^2\alpha + rL_{ns}(r) - A_{eff}(r) = 0, \tag{36}$$

to solve for the principal r=r_e. The article of Lindquist [46] is devoted to a discussion of the solution of 36 for cross sections of arbitrary, simply connected polygonal shape. The solution provides a model for penetration of a non-wetting fluid through the throat separating two pores and become of primary importance in network models of two-phase flow. In addition to providing entry pressure conditions for each throat, the solution quantifies details of the wetting fluid films occurring in corners such as β_i- throat corner half-angles,

68
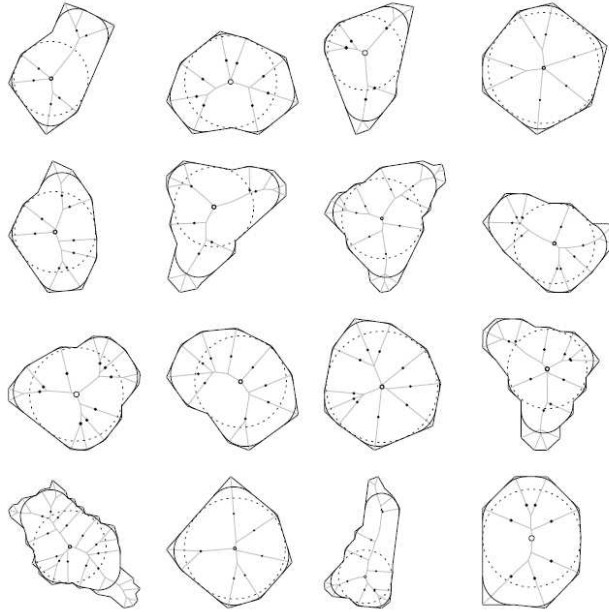
Figure 24: Arc meniscus locations (solid arcs) at entry pressure for $\theta=0$ for the first 16 throats analyzed in the 22% porosity Fontainebleau core sample image. Solid points indicate centers of the curvature of menisci. The dashed circle is the maximally described circle, centered at the root location of the MA. (W. B. Lindquist, 2006)

A_{wi} - wetting phase corner/vertex areas. Such films provide critical pathways for wetting fluid movement [46]. Fig. 24 shows solutions of 36. In order to construct the MA for the interior of each throat Held's Vroni software package [48] was used and modified by adding a bisection algorithm to compute the solution to 36 by Lindquist.

We also present the cumulative porosity and pore entry pressure distribution curves Fontainebleau sandstone for 7.5%, 13%, 15% and 22% porosity cores in Fig. 26.

In the case of 7.5% porosity sample the cumulative porosity curve provides proof of the large fraction of small pores (high entry pressure) compared to other samples with larger porosity. Pore entry pressure distribution for

Figure 25: The overall saturation of corner filaments versus average saturation in drainage of Fontainebleau sandstone for 15% and 22% porosity cores.

Figure 26: The cumulative porosity and pore entry pressure distributions curves computed from Fontainebleau sandstone samples of 7.5%, 13%, 18% and 22% bulk porosity from top to bottom respectively.

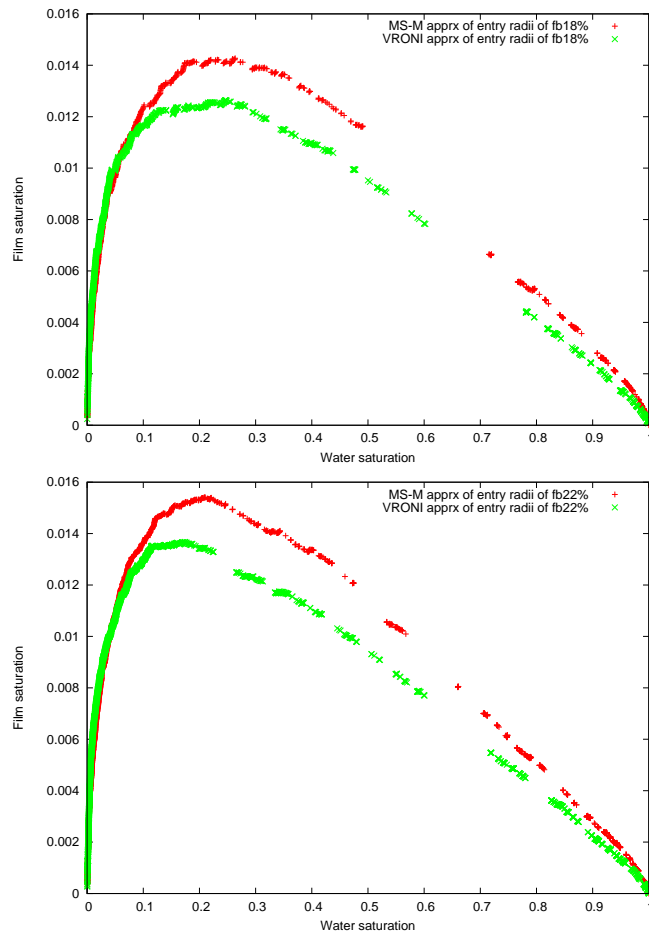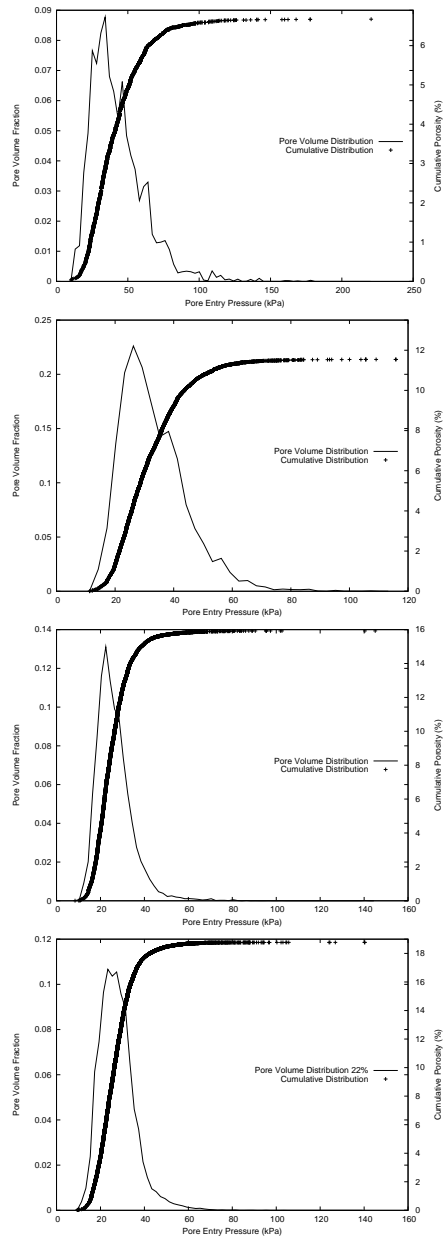7.5% sample is relatively wide and skewed to the right towards higher entry pressures. Over an increase of porosity we observe that pore entry pressure distribution narrows and becomes more symmetric. The behavior of relative permeability curves for various porosity samples can be observed and interpreted in parallel with pore entry pressure distributions (Fig. 26) in §4.5.

4.4 Water Saturation and Hydraulic Conductances in a Single Pore

4.4.1 Water and Oil Saturations

It is important to emphasize here that all the volume of the pore network is in the pore bodies. So we solely concentrate on pores in order to compute water saturation. If a pore is filled with non-wetting phase, wetting phase forms thick films along the walls of pores in grooves and wedges. It is vital to quantify the amount of water and so the amount of oil in a single pore throughout the drainage process: as capillary pressure increases, oil squeezes water out and so water volume in a pore changes. Since water is present as arc meniscii (AM's) in the corners, we utilize Held's Vroni software package [48] for computing dimensionless total throat wetting area $A_w \equiv \frac{1}{tan(\beta_i)} - \alpha_i$ where β_i is the half angle of the vertex i and α_i is the half angle of the meniscus in vertex i. The details of an arbitrary throat geometry are in [45]. It is important to note that throat wetting area is computed using actual throat geometry and therefore is more accurate compared to a wetting area of a triangular throat. Multiplying A_w by the radius of arc meniscus (r) squared we get dimensional throat wetting area for arbitrary capillary pressure ($P_c = \gamma_{nw}/r$). The drawback is that we do not compute water volume in a single pore using actual pore surface which can be a future extension to our work. Instead, the volume of water is estimated

to be the fraction of the cross section occupied by the phase multiplied by the total pore body volume. To compute the fraction, we average wetting areas of throats connected to the pore and divide it by the average pore cross section area. The overall saturation of each phase is found by adding the volume of each phase in every pore body and dividing by the total pore volume of the network.

4.4.2 Water Corner Conductance

The conductances of oil and water when both fluids are present in a single pore are computed following the work of Oren *et al.* [62] and Patzek [65]. Here we again introduce a channel notion discussed in §3.1. However if a throat together with two adjoining pores completely filled with water, the hydraulic conductance of an associate channel is computed using Lattice-Boltzmann conductance. In case when a channel shares two fluids, each fluid channel hydraulic conductance is based upon series resistance. The hydraulic conductance of a throat is computed via 37:

$$g_{w,i} = \frac{r^2 A_{w,i}}{C_{w,i}\mu_w}[62],\tag{37}$$

where r is the radius of curvature, $A_{w,i}$ is the corner i area of wetting film, μ_w is water viscosity (cp), and $C_{w,i}$ is a dimensionless flow resistance factor that accounts for the reduced water conductivity close to the pore walls. Numerical solutions of the corner flow problem show that C_w depends on the corner geometry, the contact angle, and the boundary condition at the oil/water interface [62]. Ransonoff *et al.* [72] studied the problem of low Reynolds number wetting liquid flow in a non-circular capillary and separated this problem into individual corner flow problems and solved numerically. The solution is presented in terms of a dimensionless flow resistance C_w and tabulated as a function of corner geometry, surface shear viscosity, and a contact angle, which is in our case

$\theta=0$. So, we need only to choose the correct surface shear viscosity η which affects the boundary condition at the interface. As mentioned earlier in this work, we use no-slip boundary condition at the rigid interface, so $\eta = \infty$. The total throat hydraulic conductance is the sum of all the corner conductances.

The hydraulic conductance of a pore is computed using Eq. 37. A pore is approximated as a triangular duct based on its shape factor, computed from 12 in section §3.1. The effective length l_c is determined the same way as in a single-phase model.

4.4.3 Oil Center Conductance

Since non-wetting phase occupies the center of a pore/throat body, the oil pore/throat conductance is estimated from

$$g_o = \frac{3r^2 A_o}{20\mu_o}[62],$$

(38)

where A_o=A-A_w, A is the throat area, A_o, A_w are areas of oil and water respectively, μ_o is the viscosity of oil and r is the radius of curvature. Pores are estimated as triangular ducts.

4.5 Interpretation of Results

The non-wetting phase relative permeability curves k_{ro} show two types of behavior: in the first (highly heterogeneous), they take the conventional S-shape curve, while in the second case (homogeneous case) the absence of any plateau in the low saturation zone is noted. It is seen from Fig. 27 that as the porosity decreases, k_{ro} curve tends to flatten out. This fact can be explained by looking at Fig. 26 and noting that pore entry pressure distribution of 7.5% porosity sample is skewed to the right depicting large fraction of small pores with high entry pressure. As the 7.5% porosity sample becomes desaturated,

74

the smaller pores are invaded with non-wetting fluid and therefore take part in non-wetting fluid flow without greatly modifying its permeability but remarkably enough changing water saturation. As porosity increases, Fontainebleau samples have a more uniform porosity and k_{ro} values remain small until lower water saturation (each higher porosity curve is located below lower porosity curve in Fig. 28).

One curious observation (see Fig. 29) is that the permeability curves for the wetting fluid are more or less aligned near each other except 7.5% porosity sample which is found to be more heterogeneous with non-uniform porosity. This indicates that the characteristic pore space geometry is a more important factor for the relative permeability estimates than the porosity and in fact, pore volume and pore entry pressure distributions are similar for 13%, 15% and 22% porosity samples.

A knowledge of how the capillary pressure is related to saturation in a porous medium, the capillary pressure curve, is useful to characterize the pore structure of the medium and to predict how one phase displaces the other [16]. It is also used in the study of the capillary pressure versus saturation relationship in dependence on the contact angle and a direction of the displacement process. Usually capillary pressure curves are derived experimentally either from nuclear magnetic resonance (NMR) pore size distributions or from mercury porosimetry intrusion tests and applied as input file in numerical reservoir simulation.

As is apparent from Fig. 30, increasing P_c at first results only in a very small change in saturation. In this initial phase of the simulation the non-wetting phase has penetrated only pores at or near the surface of the sample but soon the P_v versus S_w curve stabilizes, getting flat, until it becomes vertical again at low saturation values. Since we use the assumption that wetting phase keeps a continuous network throughout the primary drainage process, no

Figure 27: Relative permeability curves for two fluids computed from Fontainebleau sandstone samples of 7.5%, 13%, 18% and 22% bulk porosity.

Figure 28: Comparison of oil relative permeability curves computed from Fontainebleau sandstone samples of 7.5%, 13%, 18% and 22% bulk porosity.
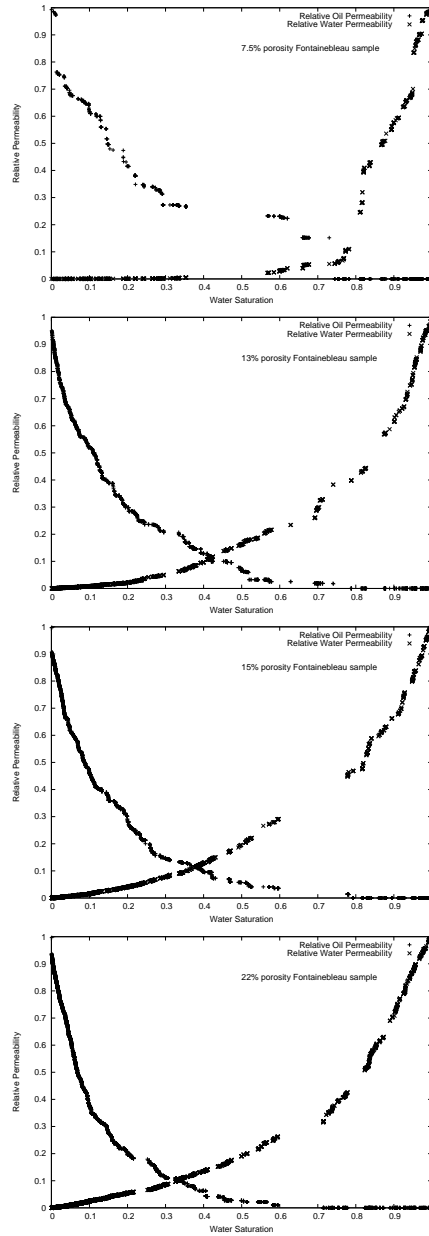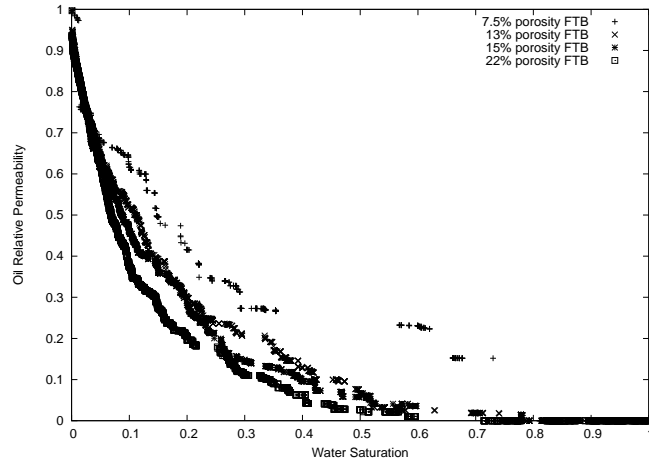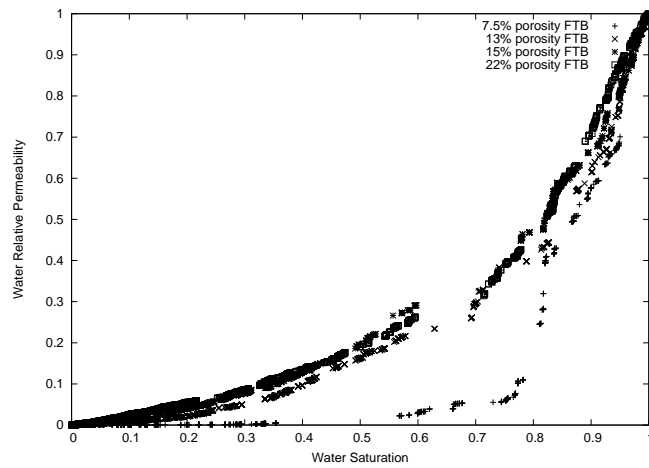

Figure 29: Comparison of water relative permeability curves computed from Fontainebleau sandstone samples of 7.5%, 13%, 18% and 22% bulk porosity.
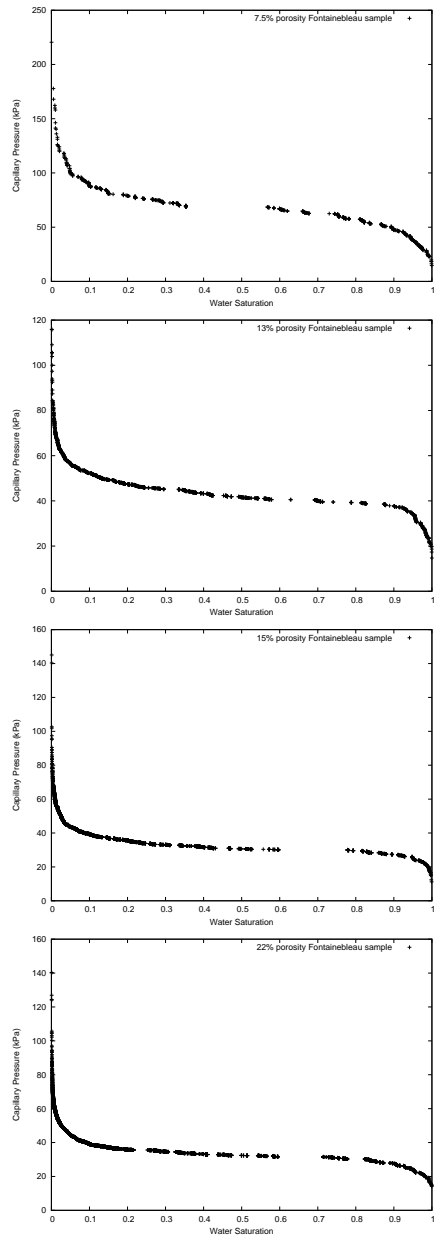
Figure 30: Primary drainage capillary pressure versus water saturation curves computed from Fontainebleau sandstone samples of 7.5%, 13%, 18% and 22% bulk porosity.

78
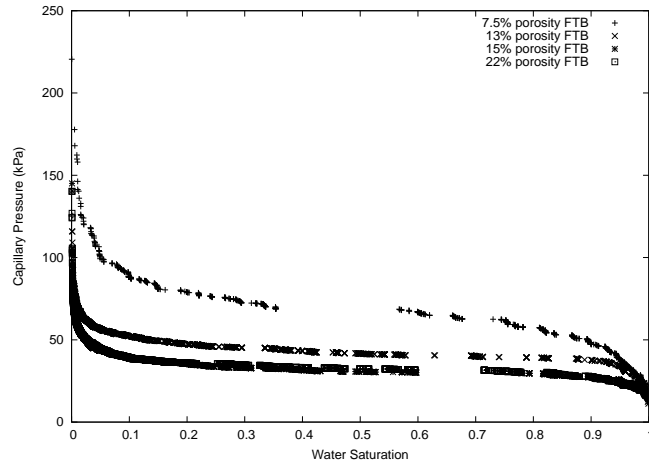
Figure 31: Comparison of capillary pressure curves computed from Fontainebleau sandstone samples of 7.5%, 13%, 18% and 22% bulk porosity.

trapped wetting phase can be observed in Fig. 30 and therefore an "irreducible" wetting phase saturation is almost zero. It is shown experimentally that a wetting phase is not trapped in a sandstone and ,probably, in most natural water-wet porous media because the grooves, edges, and wedges on the pore surface. After the non-wetting phase has penetrated the central part of a pore there is always wetting fluid left in the surface grooves, etc, in the form of 'thick' films [21]. The shape of capillary pressure curves for various porosity (Fig. 31) can be explained by the shape of pore entry pressure distributions (Fig. 26): the wider pore entry pressure distribution, the bigger the slope of capillary pressure curve.

The experimental methods used to analyze fluid transport through porous media vary greatly: mercury porosimetry, electrical conductivity, nuclear magnetic resonance, acoustic properties of the medium to name a few. These experiments typically have large uncertainties, and the measured permeabilities often depend on minute experimental details. Carrying out the experiments as for example the water-flow through low-porosity rock samples is very time

consuming. In addition to the permeability itself, many material characteristics on which the measured permeability depends, can be difficult to determine accurately.

A great deal of literature that describes the generic properties of Fontainebleau sandstone (see Chap. §2) exists. However relatively few attempts have been made to predict petrophysical properties quantitatively. In fact, there has been a paucity of network studies incorporating any experimental data at all. Experimental data is scarce. In this study we compared our simulated relative permeability curves for samples of 13%, 15% and 22% porosity with experimental curves of Sorbie *etal*. [56]. Experimental reservoir rock samples are taken from a fairly clean homogeneous well-sorted sandstone plugs from a shallow marive depositional environment and are similar to Fontainebleau sandstone. We were unable to get numerical data from the authors due to a non-disclosure agreement, so we can only make a qualitative comparison. In in Fig. 32 we show the experimental curves (blue) extracted from their paper and the results of our compution (black) for each porosity sample. We believe that the agreement that we get is a very good indication that our novel computational methods very accurately describe the primary drainage process.

In Fig. 33 we demonstrate the invasion process of non-wetting fluid into 7.5 % porosity sample using Geomveiw 3D Visualization software. The marching cubes algorithm provides interphase surface to the voxel resolution level, and only limited number of triangles can be displayed due to several constraints such as random-access memory (RAM) and a memory capacity of a video card. While great voxel level detail is important for area computation, we might be interested in the relative position of that non-wetting fluid in the volume. For such a purpose, visualizing a reduced number of triangles (which is a common transformation on triangulated meshes) would be enough [70].
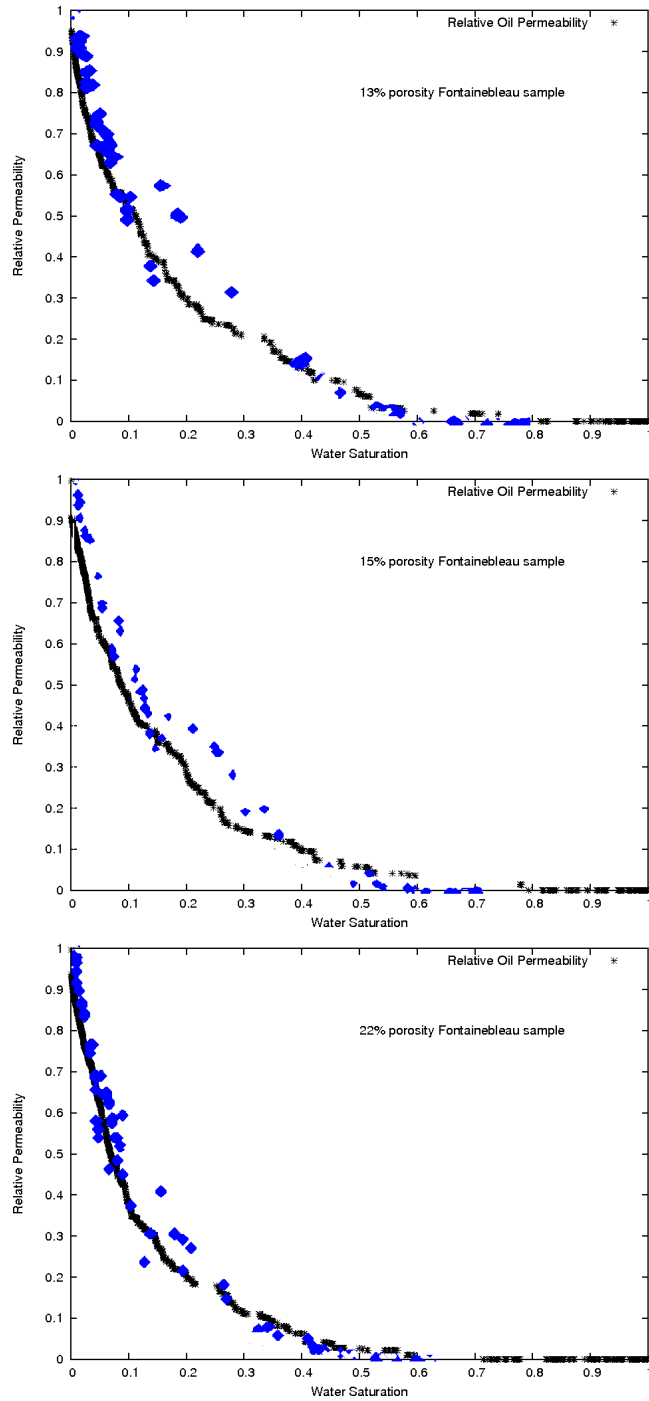
Figure 32: Comparison of experimental relative permeability curves (blue) obtained by Sorbie [56] with our computation (black) for Fontainebleau sandstone 13%, 18% and 22% bulk porosity samples.
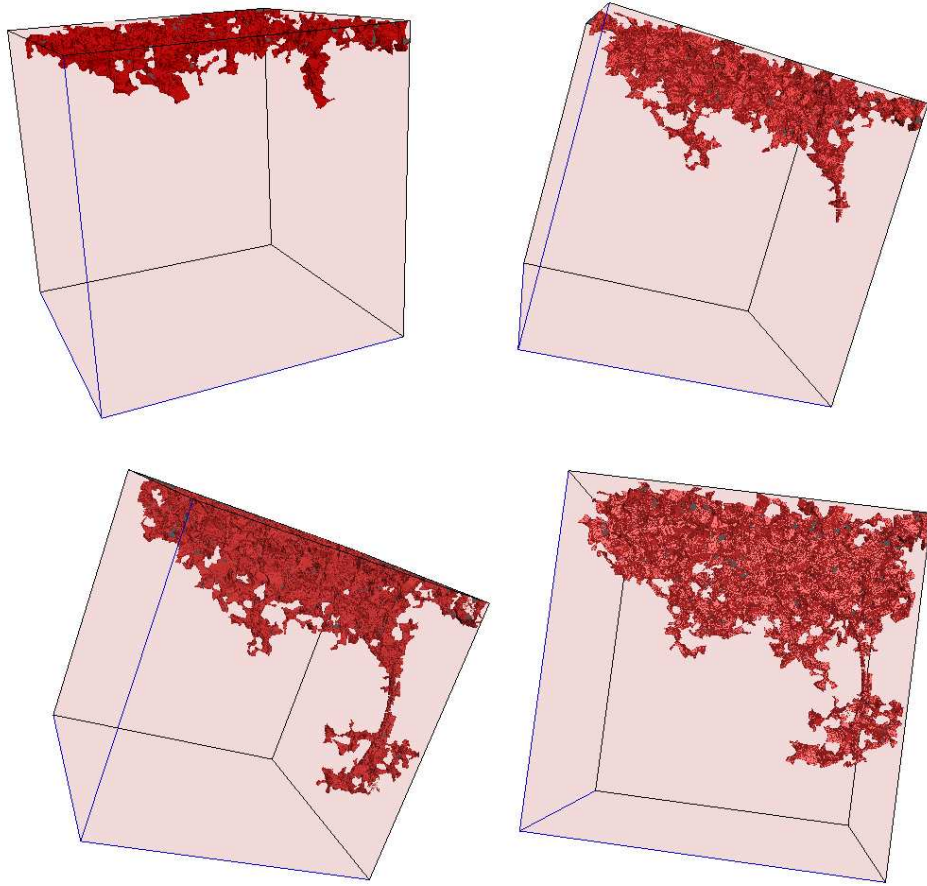
Figure 33: Geomview plots depicting invasion of non-wetting fluid into a 7.5% porosity Fontainebleau sample. Non-wetting fluid is red.

In §5 we address this problem as a future extension of our work.

Chapter 5

Discussion

We have developed single-phase and multi-phase network models capturing essential pore characteristics for predicting hydraulic properties used in reservoir simulations. Our sensitivity study indicates that single-phase network flow models utilizing series resistance computations for pore-to-pore conductance are capable of "tuning" bulk absolute permeability values over at least one order-of-magnitude. Our results show that a "tuned" model will produce sharp bulk values only over a limited range of porosity.

By comparing with lattice Boltzmann computations, our results indicate that network flow models employing channel conductances based upon shape factor do not capture a sufficiently rapid increase of conductance with increasing shape factor. We have extracted a power law model appropriate for Fontainebleau sandstones which, more accurately, captures this trend.

The NF-LBC hybrid network flow - lattice Boltzmann model that we have introduced encorporates advantages of both methods. The lattice Boltzmann simulations are run locally, and in a highly parallelizable fashion, to provide pore-to-pore conductances for input into a network flow model. This hybrid model eliminates the need for series resistance conductance computations, and utilizes the superior ability of the lattice Boltzmann simulations to capture

individual channel geometry.

The modified NF-LBG model, which requires only estimates for throat shape factors and the two parameters appearing in (17), should enable more accurate computations in "artificial" medium models, i.e. those not based upon a specific 3D realization.

Two-phase model for primary drainage incorporates the throat real geometries for computing throat entry pressures, water saturations and water conductances. Absolute permeability used in two-phase model is computed via the NF-LBC model. The relative permeability curves of water and oil are analyzed for four samples of Fontainebleau sandstone with various porosities. The shapes of relative permeability curves linked to pore characteristics which define hydraulic behavior. It is shown that the oil relative permeability curves for Fontainebleau sandstone have a convex-like shape and therefore displaying the homogeneity of pore space. The permeability curves for the wetting fluid are aligned near each other indicating that the characteristic pore space geometry is a more important factor for the relative permeability estimates than the porosity.

We identify the following as the future extensions of our work:

- To improve th calculation of water saturation and water and oil conductances by considering the actual pore surface for water volume calculation and extending Lattice-Boltzmann channel model (NF-LBC) to two-phase channel model. It is vital to note that for the computation of water/oil conductances only channel actual geometry is needed for accurate predictions and 3DMA-Rock software provides with actual pore space description. Such improvement will enhance predictive capabilities of two-phase network as it simulates primary drainage or secondary imbibition.

- To study of the role of contact angle. So far we analyzed Fontainebleau

sandstone which is completely water-wet with zero contact angle. Most porous rocks exhibit mix-wetting and therefore it is inevitable to build a two-phase pore network which take as input an arbitrary contact angle. Having included a simulation of mixed-wet system one can study the amount of trapping of the wetting phase in primary drainage and imbibition.

- To include imbibition into two-phase network model. The microscopic picture of imbibition in porous media is much more complicated than that of drainage. Such factors as contact angle hysteresis, oil trapping, oil clusters tracking and various throat filling scenarios should be considered and the wealth of information provided by 3DMA-(R)ock should be incorporated to extend predictive capabilities to network models investigated at other research groups.

- To simulate two phase flow via LBM [76, 53] in the exact throat and pore geometries in order to predict relative permeabilities to oil and water. Then we could compare network flow with LB results and identify which pore space characteristic parameters play a crucial role in two-phase flow.

- To use of improved visualization methods. Both processes, primary drainage and secondary imbibition, could be visualized and so one could see both fluids' evolution through time steps and its distribution in pore space, track oil clusters and identify trapped water/oil blobs. For such a purpose, visualizing a reduced number of triangles (which is a common transformation on triangulated meshes) would be enough. Therefore, it would be beneficial if 3DMA-Rock incorporated a preexisting library functions operating on of triangulated surfaces such as CGAL [40] or GTS [41].

Bibliography

[1] 3DMA-Rock. http://www.ams.sunysb.edu/~lindquis/3dma/3dma_rock/3dma_rock.html.

[2] A. Al-Futaisi and T.W. Patzek. The impact of wettability alteration on two-phase flow characteristics of sandstones: A quazi-static description. *Water Resources Rsearch*, pages 1–10, 2002.

[3] C. Arns, M.A. Knackstedt, W.V. Pinczewski, and W.B. Lindquist. Accurate estimation of transport properties from tomographic images. *Geophysical Research Letters*, 28:3361–3364, 2001.

[4] J. Arns, C. Arns, A. Sheppard, R. Sok, M. Knackstedt, and W. Pinczewski. Relative permeability from tomographic images; effect of correlated heterogeneity. *J. of Petroleum Science and Engineering*, 39:247–259, 2003.

[5] S. Bakke and P.E. Øren. 3-D pore-scale modeling of sandstones and flow simulations in the pore networks. *SPE J.*, 2:136–149, 1997.

[6] J. Bloomenthal. Polygonization of implicit surfaces. *IEEE Comput. Graph. Appl.*, 5:341–355, 1988.

[7] M.J. Blunt. Flow in porous media - pore-network models and multiphase flow. *Current Opinion Colloid Interface Sci.*, 6:197–207, 2001.

[8] M.J. Blunt, M.D. Jackson, M. Piri, and P.H. Valvatne. Detailed physics, predictive capabilities and macroscopic consequences for pore-network models of multiphase flow. *Adv. Water. Resour.*, 25:1069–1089, 2002.

[9] M.J. Blunt, M.J. King, and H. Scher. Simulation and theory of two-phase flow in porous media. *Phys. Rev. A*, 46:7680–7699, 1992.

[10] M.J. Blunt and H. Scher. Pore-level modeling of wetting. *Phys. Rev. E*, 52:6387–6403, 1995.

[11] T. Bourbie, O. Coussy, and B. Zinszner. *Acoustics of Porous Media*. Gulf Publishing Co., Paris, France, 1987.

[12] T. Bourbie and B. Zinszner. Hydraulic and acoustic properties as a function of porosity in fontainebleau sandstone. *J. Geophys. Res.*, 90:11524–11532, 1985.

[13] S. Bryant and M.J. Blunt. Prediction of relative permeability in simple porous media. *Physical Review A*, 46:2004–2011, 1992.

[14] M.A. Celia, P.C. Reeves, and L.A. Ferrand. Recent advances in pore-scale models for multiphase flow in porous media. *Rev. Geophys. Suppl.*, 33:1049–1057, 1995.

[15] C. Chen, A.I. Packman, and JF. Gaillard. Pore-scale analysis of permeability reduction resulting from colloid deposition. *Geophys. Research Letters*, 35, 2008.

[16] M.C. Cunha and A.C. Moretti. Calculating capillary pressure curve from single-speed centrifuge experiments. *Inverse Problems*, 16:1897–1906, 2000.

[17] H.K. Dahle and M.A. Celia. A dynamic network model for two-phase immiscible flow. *Computat. Geosci.*, 1:1–22, 1999.

[18] E. Dana and F. Skoczylas. Gas relative permeability and pore structure of sandstone. *Int. Journal of Rock Mechanics and Mining Sciences*, 36:613–625, 1999.

[19] P.G. de Gennes. Percolation - a new unifying concept. *La Recherche*, 7:919–926, 1980.

[20] D. d'Humiéres. Generalized lattice Boltzmann equations. *Prog. Astonat. Aeronaut.*, 159:450–458, 1992.

[21] F.A.L. Dullien. *Porous Media: Fluid Transport and Pore Structure*. Academic press, 2 edition, 1992.

[22] I. Fatt. The network model of porous media I. Capillary characreristics. *Pet. Trans. AIME*, 207:144–159, 1956a.

[23] I. Fatt. The network model of porous media II. Dynamic properties of a single size tube network. *Pet. Trans. AIME*, 207:160–163, 1956b.

[24] I. Fatt. The network model of porous media III. Dynamic properties of networks with tube radius distribution. *Pet. Trans. AIME*, 207:164–181, 1956c.

[25] J.T. Fredrich, A.A. DiGiovanni, and D.R. Noble. Predicting macroscopic transport properties using microscopic image data. *Journal of Geophys. Research*, 111, 2006.

[26] X. He and G. Doolen. Lattice Boltzmann method on curvilinear coordinate system: Flow around circular cylinder. *J. Comput. Phys.*, 134:306, 1997.

[27] X. He, G. Doolen, and T. Clark. Comparison of the lattice boltzmann method and the artificial compressibility method for navier-stokes equations. *Journal of Computational Physics*, 179:439 – 451, 2002.

[28] R.J. Held and M.A. Celia. Pore-scale modeling extension of constituitive relationships in the range of residual saturations. *Water Resour. Res.*, 37:165–170, 2001.

[29] M. Honarpour and D. Maloney. Relative permeability technology and applications. 1990.

[30] S.K. Hwang. *Z. Physik. Chemie Neue Folge.*, 105, 1977.

[31] M.A. Ionnidis and I. Chatzis. A mixed-percolation model of capillary hysteresis and entrapment in mercury porosimetry. *J. Colloid Interf. Sci.*, 161:278–291, 1993.

[32] M.A. Ionnidis and I. Chatzis. Network modeling of pore structure and transport properties of porous media. *Chem. Engin. Sci.*, 48:951–972, 1993.

[33] G. Jin, C. Torres-Verdin, F. Radaelli, and E. Rossi. Experimental validation of pore-level calculations of static and dynamic petrophysical properties of clastic rocks. 11-14 November 2007.

[34] P.P. Jonker. Morphological operations on 3d and 4d image: from shape primitive detection to skeletonization. pages 371–391, December 13-15 2000.

[35] P.P. Jonker and A.M. Vossepoel. On skeletonization algorithms for 2,3 ... n dimensional images. pages 71–80, October 4-6 1994.

[36] M.A. Knackstedt, A.P. Sheppard, and W.V. Pinczewski. Simulation of mercury porosimetry on correlated grids: Evidence of extended correlated heterogeneity at the pore scale. *Phys. Rev. E*, 58:R6923–R6926, 1998.

[37] M.A. Celia L. Li, C.A. Peters. Upscaling geochemical reaction rates using pore-scale network modeling. *Adv. Water Resourc.*, 29:1351–1370, 2006.

[38] P. Lallemand, , and L.-S. Luo. Theory of the lattice Boltzmann method: Dispersion, dissipation, isotropy, galilean invariance, and stability. *Phys. Rev. E*, 68:036706, 2000.

[39] T.C. Lee, R.L. Kashyap, and C.N. Chu. Building skeleton models via 3d medial surface/axis thinning algorithms. *Graph Mod Image Process*, 56:462–478, 1994.

[40] Computational Geometry Algorithms Library. http://www.cgal.org/.

[41] GNU Triangulated Surface Library. http://gts.sourceforge.net/index.html/.

[42] W. B. Lindquist. 3DMA general users manual. Technical report, Department of Applied Mathematics and Statistics, State University of New York, Stony Brook, NY, 1999.

[43] W.B. Lindquist. Network flow model studies and 3D pore structure. *Contemp. Math.*, 295:355–366, 2002.

[44] W.B. Lindquist. Quantitative analysis of three dimensional x-ray tomographic images. pages 103–115, 2002.

[45] W.B. Lindquist. The geometry of primary drainage. *J. Colloid Interf. Sci.*, 296:655–668, 2006.

[46] W.B. Lindquist and A.B. Venkatarangan. Investigating 3D geometry of porous media from high resolution images. *Phys. Chem. Earth. A*, 25:593–599, 1999.

[47] W.B. Lindquist, A.B. Venkatarangan, J. Dunsmuir, and T. f. Wong. Pore and throat size distributions measured from synchrotron X-ray tomographic images of fontainebleau sandstones. *J. Geophys. Res.*, 103:21508–21528, 2000.

[48] Vroni M. Held. http://www.cosy.sbg.ac.at/∼held/projects/vroni/vroni.html.

[49] Z. Karpyn M. Piri. *Phys. Rev.*, E 76 (1):016316, 2007.

[50] S.X. Ma, G. Mason, and N.R. Morrow. Effect of contact angle on drainage and imbibition in regular polygonal tubes. *Colloids Surf.*, A 117:273–291, 1996.

[51] C. Manwart, A. Koponen, U. Aaltosalmi, R. Hilfer, and J. Timonen. Lattice-Boltzmann and finite-difference simulations for the permeability of three-dimensional porous media. *Phys. Rev. E*, 66:016702, 2002.

[52] C. Manwart and R.Hilfer. Numerical simulations of creeping fluid flow in reconstructed models of porous media. *Physica A*, 314:706 – 713, 2002.

[53] N. S. Martys and J. G. Hagedorn. Multiscale modeling of fluid transport in heterogeous materials using descrete boltzmann methods. *Materials and Structures*, 35:650–659, 2002.

[54] G. Mason and N.R. Morrow. Capillary behavior of a perfectly wetting liquid in irregular triangular tubes. *J. Colloid Interf. Sci.*, 141:262–274, 1991.

[55] R.P. Mayer and R.A. Stowe. Mercury porosimetry-breakthrough pressure for penetration between packed spheres. *J. Colloid Interface Sci.*, 20:893–911, 1965.

[56] S. McDougall, J. Cruickshank, and Ken S Sorbie. Anchoring methodologies for pore-scale nentwork models: Application to relative permeability and capillary pressure prediction. 2001.

[57] R. Mei, L-S. Luo, and W. Shyy. An accurate curved boundary treatment in the lattice Boltzmann method. *J. Comput. Phys.*, 155:307–330, 1999.

[58] R. Mei, W. Shyy, D. Yu, and L-S. Luo. Lattice Boltzmann method for 3-D flows with curved boundary. *J. Comput. Phys.*, 161:680–699, 2000.

[59] J.J. Monaghan. An introduction to sph. *Computer Physics Communications*, 48:88–96, 1988.

[60] H.F. Nordhaug, H.G. Dahle, M.E. Espedal, W.G. Gray, and M.A. Celia. Two phase flow including interfacial area as a variable. pages 231–238, June 25 - 29 2000.

[61] W. Oh and W.B. Lindquist. Image thresholding by indicator kriging. *IEEE Trans. Pattern Anal. Mach. Intell.*, 21:590–602, 1999.

[62] P.E. Øren, S. Bakke, and O.J. Arntzen. Extending predictive capabilities to network models. *SPE J.*, 3:324–336, 1998.

[63] N.R. Pal and S.K. Pal. A review on image segmentation techiniques. *Pattern Recognition*, 26:1,277–1,294, 1993.

[64] C. Pan, L.-S. Luo, and C.T. Miller. An evaluation of lattice Boltzmann equation methods for simulating flow through porous media. In *Computational Methods in Water Resources 2004 Conference Proceedings*, June 2004.

[65] T. Patzek. Verification of a complete pore network simulator of drainage and imbibition. April 2000.

[66] T.W. Patzek and D.B. Silin. Shape factor and hydraulic conductance in noncircular capillaries. *J. Colloid Interf. Sci.*, 236:295–304, 2001.

[67] H.M. Princen. Capillary phenomena in assemblies of parallel cylinders I. Capillary rise between 2 cylinders. *J. Colloid Interface Sci.*, 30:69–75, 1969.

[68] H.M. Princen. Capillary phenomena in assemblies of parallel cylinders II. Capillary rise in systems with more than 2 cylinders. *J. Colloid Interface Sci.*, 30:359–371, 1969.

[69] H.M. Princen. Capillary phenomena in assemblies of parallel cylinders III. Liquid columns between horizontal parallel cylinders. *J. Colloid Interface Sci.*, 34:171–184, 1970.

[70] M. Prodanovic. PhD thesis, State University of New York at Stony Brook, 2005.

[71] M. Prodanovic, W.B. Lindquist, and R.S. Seright. Porous structure and fluid partitioning in polyethylene cores from 3d x-ray microtomographic imaging. *J. Colloid Interf. Sci.*, 298:282–297, 2006.

[72] T.C. Ransonoff and C.J. Radke. Laminar flow of a wetting liquid along the corners of a predominantly gas-occupied noncircular pore. *Journal of Colloid and Interface Science*, 121:392–401, 1988.

[73] P.C. Reeves and M.A. Celia. A functional relationship between capillary pressure, saturation, and interfacial area as revealed by a pore scale network model. *Water Resour. Res.*, 32:2345–2358, 1996.

[74] H. Salem and G. Chilingarian. Influence of porosity and direction of flow on tortuosity in unconsolidated porous media. *Energy Sources*, 22:207–213, 2000.

[75] R.S. Seright, J. Liang, W.B. Lindquist, and J.H. Dunsmuir. Use of X-ray computed microtomography to understand why gels reduce permeability to water more than to oil. *J. Petroleum Sci. Eng.*, 39:217–230, 2003.

[76] X. Shan and H. Chen. Lattice boltzmann model for simulating flows with multiple phase and components. *Phys. Rev. E*, 47:1815–1819, 1993.

[77] H. Shin. *A Throat Finding Algorithm for Medial Axis Analysis of 3D Images of Vesiculated Basalts*. PhD thesis, Stony Brook University, 2002.

[78] H. Shin, W.B. Lindquist, D.L. Sahagian, and S.-R. Song. Analysis of the vesicular structure of basalts. *Computer Geosci.*, 31:473–487, 2005.

[79] D. Silin and T. Patzek. Pore space morphology analysis using maximal inscribed spheres. *Physica A*, 371:336–360, 2006.

[80] D.B. Silin, G. Jin, and T. Patzek. Robust determination of the pore space morphology in sedimentary rocks. 5-8 October 2003.

[81] R. M. Sok, M. A. Knackstedt, A. P. Sheppard, W. V. Pinczewski, W. B. Lindquist, A. Venkatarangan, and L. Paterson. Direct and stochastic generation of network models from tomographic images; effect of topology on two phase flow properties. *Transport Porous Media*, 46:345–371, 2002.

[82] P. Spanne, J. F. Thovert, C. J. Jacquin, W. B. Lindquist, K. W. Jones, and P. M. Adler. Synchrotron computed microtomography: Topology and transports. *Phys. Rev. Lett.*, 73:2001–2004, 1994.

[83] S. Succi. *The Lattice Boltzmann Equation for Fluid Dynamics and Beyond*. Clarendon Press, Oxford, 2001.

[84] A. Tartakovsky and P. Meakin. Modeling of surface tension and contact angles with smoothed particle hydrodynamics. *Physical Review E*, 72.

[85] H. Thiesel. Exact isosurfaces for marching cubes. *Computer Graphics Forum*, 21:19–31, 2002.

[86] Ѳ.D. Trier and A.K. Jain. Goal-directed evaluation of binarization methods. *IEEE Trans. Pattern Analysis and Machine Intelligence*, 17:246–258, 1997.

[87] P. Valvatne and M. J. Blunt. Predictive pore-scale network modeling. October 2003.

[88] P.H. Valvatne and M.J. Blunt. Predictive pore-scale modeling of two-phase flow in mixed wet media. *Water Resour. Res.*, 40:W07406, 2004.

[89] A.B. Venkatarangan. *Geometric and Statistical Analysis of Porous Media*. PhD thesis, State University of New York at Stony Brook, 2000.

[90] R. Verberg and A.J.C. Ladd. Simulation of low-Reynolds-number flow via a time-independent lattice-Boltzmann method. *Phys. Rev. E*, 60:3366–3373, 1999.

[91] R. Verberg and A.J.C. Ladd. Lattice-Boltzmann model with sub-grid-scale boundary conditions. *Phys. Rev. Lett.*, 84:2148, 2000.

[92] M. Piri Z. Karpyn. *Phys. Rev.*, E 76 (1):016315, 2007.